UNIVERSITY OF CALIFORNIA
SANTA CRUZ

HIGH ENERGY ATMOSPHERIC PHYSICS OF THE TERRESTRIAL GAMMA RAY FLASH WITH MULTI-WAVELENGTH OBSERVATIONS

A dissertation submitted in partial satisfaction of the
requirements for the degree of

DOCTOR OF PHILOSOPHY

in

PHYSICS

by

Jeffrey M. Chaffin

December 2022

The Dissertation of Jeffrey M. Chaffin
is approved:

Professor David M. Smith, Chair

Professor Mike Hance

Ken Eack, Ph.D.

Peter Biehl
Vice Provost and Dean of Graduate Studies

Table of Contents

List of Figures

Abstract

High Energy Atmospheric Physics of the Terrestrial Gamma Ray Flash with Multi-Wavelength Observations

by

Jeffrey M. Chaffin

X-ray and gamma-ray emissions from storm clouds and lightning are routinely emitted over timescales from microsecond bursts of x-rays associated with lightning leaders and sub-millisecond bursts of gamma-rays called terrestrial gamma-ray flashes (TGFs) to seconds long 'glows' of gamma radiation. The focus of this dissertation will be on the physics and analysis of TGFs. To begin, I will review the physics of thundercloud charging, lightning initiation and the propagation of lightning leader channels. Understanding the varied electric field environments of these thunderstorm processes is important context to understanding the TGF mechanism and the prevailing theories of TGF production. I will give an overview of the current understanding of TGF physics detailing those competing theories and the prevailing questions for future research. From the experimental perspective I will discuss TGF distribution trends using observations by orbiting spacecraft as well as give a summary of the use of low frequency lightning radio sferics; how they are used to provide location data for TGF analysis and more recently the importance of multi-wavelength measurements of the TGFs current moment to increase our understanding of the TGF-lightning leader relationship.

This introduction will be followed by two soon to be published papers on TGF observations and coincident radio sferic data. The first paper will focus on an observation of a possible reverse beamed TGF by the Gamma-Ray Burst Monitor aboard the Fermi spacecraft. This is a follow up paper on Pu et al. (2020), who published the coincident radio sferic data along with the Fermi gamma-ray observation proposing the possibility the observation was the reverse beam component of a downward TGF associated with a -CG lightning event initiating at 6km. I investigate this possibility with an in depth analysis of the gamma-ray data using Monte Carlo simulations, meteorological analysis of the storms charge structure and updated analysis of the radio data in cooperation with the original authors.

The second paper is the publication of three new TGF observations made by a gamma-ray instrument deployed by my research group to the summit of Mt. Säntis in Switzerland. Three TGFs were observed during the 2021 summer storm season. Each TGF was coincident with a unique radio sferic, two of which have been associated with orbital TGF observations in the past. I conclude this dissertation with a summary of my instrumentation work, my current hardware projects and how my future research plans and goals are coming into focus.

Acknowledgements

I would like to express my deepest gratitude to my faculty advisor Dr. David Smith.

Many thanks also to my dissertation committee.

Lastly, I need to thank my wife Kit.

I could not have undertaken this journey without you.

Section 1

Introduction

1.1 Storm Cloud Charging and Lightning

The fundamental physics of any electric field is separation of charge. In a storm cloud this manifests as areas in the cloud where there is a strong net population of one type of charge opposed to an area of the opposite charge. This binary charge distribution requires a mechanism of charge separation where charge is transferred between particulates in the air in a preferential manner. This primary charge transfer mechanism is referred to as triboelectrification and involves collisions between soft hail (graupel) particles that are heavy enough to fall or remain stationary in the thunderstorm's updrafts and small crystals of ice that are light enough to be carried upward [Rakov and Uman, 2003]. Once the charge has been transferred between the ice and hail particles, the ice crystals are carried to upper portions of the thundercloud, while the hail falls or remains in the lower portion of the cloud. The polarity and degree of charge

transfer is determined by the conditions inside the thunderstorm at the time of the collision, notably temperature and liquid water content. This idealized thundercloud charge structure is illustrated in Figure 1.1, along with examples of some different types of lightning discharges. Essentially a thundercloud as an idealized charge configuration is not unlike a parallel plate capacitor, though the tri-pole model is thought to be a more accurate depiction. In either case it is understood that these oversimplifications of the charge structure are useful on a macro scale in determining likely storm polarities and charge center altitudes.

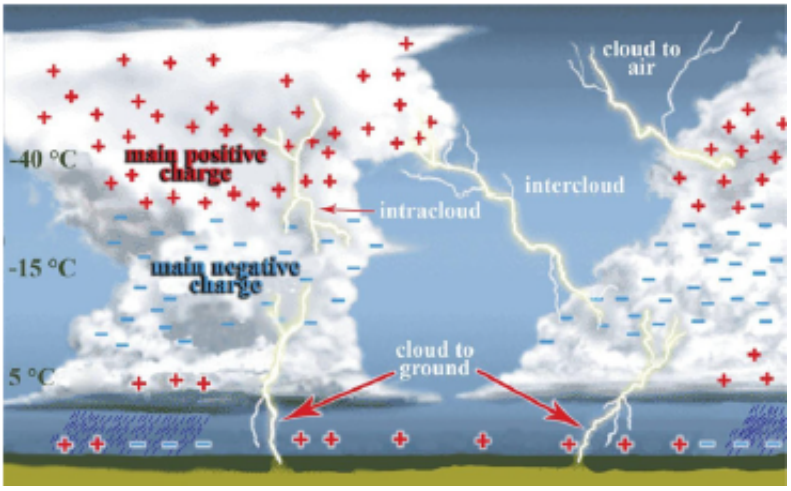

Figure 1.1: The charge structure of two simple isolated thunderclouds and some of the locations where the lightning can occur. Source: Dwyer and Uman, 2014

How lightning is initiated within these electric fields is actually a bit of a mystery, but the following mechanism must take place *somewhere* within these fields for lightning to occur. The electrical breakdown of air takes place when air changes from

an insulator to a conductor. For that to occur, there needs to be an increase in free electron concentration by ionization processes. When an electron/positive-ion pair is created in air in the presence of an electric field, the low-energy electron and the ion both move under the influence of the field. In air, the low-energy electrons will eventually undergo attachment processes, forming negative ions. This attachment time, τ, is dependent on the electric field strength and the air density. At thunderstorm altitudes, τ is usually on the order of microseconds [Dwyer and Uman, 2014]. Prior to attachment the electrons experience multiple scatters with air molecules, resulting in a constant average velocity, $\mathrm{v} = -\mu\mathrm{E}$, known as the drift velocity, where μ is the mobility of the electrons. Similarly, ions also drift in the electric field, but at a much lower speeds due to their larger masses and hence smaller mobilities.

As the electric field is increased, the average energy of the drifting electrons also increases. At strong enough fields, a fraction of the electron velocity distribution will have energies sufficient to ionize air, due to the impact of the electrons with the air molecules, thus generating additional electrons. A fraction of these secondary electrons will also ionize air, creating even more electrons. This avalanche growth in low energy electron concentration competes with the loss of electrons due to attachment. As field strength is increased the ionization rate increases rapidly, surpassing the attachment rate at about $E_{th} = 30$ kV/cm (sea level) [Dwyer and Uman, 2014], called the conventional breakdown field.

The catch is that so far there have been no electric field measurements of storm clouds that comes close to the electric field threshold for breakdown in atmosphere [Marshall and Rust, 1991; Stolzenburg et al. 2007]. There are two theories that try to account for this. The first assumes that a localized field, perhaps near a density of hydrometers (ice crystals, hail, rain drops), was sufficiently large to allow discharge to occur leading to the ionization process [Griffiths & Phelps, 1976]. An alternative explanation suggests that high energy seed electrons from cosmic rays could result in a relativistic electron avalanche (a high energy process) that jump starts the (low energy) ionization process leading to the breakdown necessary to initiate a lightning leader channel[Gurevich et al., 1992]. Regardless of how it is initiated, the electrical breakdown of air results in a thin channel of low energy or 'cold' ionized air called a streamer. The number of electrons in the avalanche grows, and the polarization of the atmosphere due to the separation of the electrons and the positive ions that trail behind will enhance the field at the front of the avalanche, increasing the amount of avalanche multiplication at the tip [V. Cooray, 2003]. Figure 1.2 illustrates the charge distribution and streamer formation process.

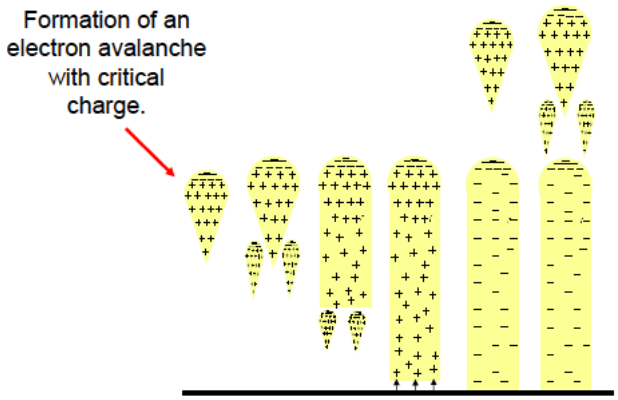

Figure 1.2: Formation of a negative streamer. Source: V. Cooray, 2003

As a streamer propagates through a strong electric field, the charge that accumulates at its tip may become sufficiently large that the streamer splits into two or more streamers. The process may repeat many times, producing a branched network of positive or negative streamers. If the currents produced by the streamers are large, the streamers may also heat the air, which increases the conductivity, allowing more current to flow, which causes more heating, and so on. This tends to constrict the current along a narrow hot channel. Specifically, above about 1500 K, the conductivity of air greatly increases due to the rapid detachment of electrons from negative ions [Dwyer and Uman, 2014]. Such hot (5000 K or more) narrow channels are referred to as leaders and they propagate in steps led by streamer formation at their head [Cooray, 2015]. When these hot channels connect two opposing charge regions (e.g., lower negative cloud and positive Earth) there is a large transfer of charge (current) discharging the background electric field. This is what is referred to as the stroke or lightning flash.

A simplified picture of a negative leader and the associated electric field amplitudes is shown in Figure 1.3. The leader propagates within an ambient background field of 1-4 kV/cm [Rakov, 2003] determined from various balloon sounding experimental data [Marshall and Rust, 1991; Stolzenburg et al. 2007]. There is a large density of negative charge that accumulates at the tip of the leader as it propagates from the streamer ionization process resulting in a non-uniform electric field of unknown extent and undetermined amplitude. Laboratory spark experiments suggest amplitudes close to the leader tip up to 300 kV/cm decreasing to 50-2 kV/cm as the distance from the tip in-

creases [Celestin and Pasko, 2015]. These inferred electric field amplitudes are integral to the understanding of the physics of TGFs.

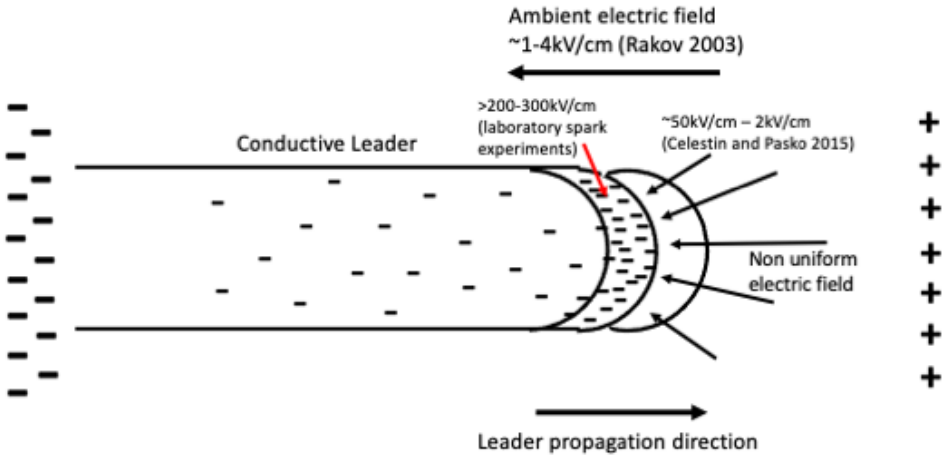

Figure 1.3: Qualitative depiction of a negative leader channel and the associated electric fields. The leader propagates through a large scale ambient background field. At the head of the leader is a high density of negative charge resulting in a large amplitude electric field within the small volume ahead of the leader tip. As the distance from the tip increases the electric field decreases. Alternately, as the distance between the leader and the positive charge center decreases the electric field leading the leader tip increases.

1.2 Terrestrial Gamma Ray Flash

Terrestrial gamma-ray flashes are thought to be the result of highly energetic (relativistic) electrons undergoing avalanche growth driven by large electric fields. These fields consist of both the background field strength of the thundercloud and transient electric fields at the tips of the previously discussed lightning leaders [Dwyer,Smith, and

Cummer, 2012]. The large populations of energetic electrons collide with atmospheric molecules, producing bremsstrahlung radiation with photon energies up to 40 MeV and minimum intensities on the order of 10^{17} photons [Dwyer and Uman, 2014]. Wilson's formulation of the runaway electron mechanism [Wilson, 1925], where he postulated the rate of energy gain of a charged particle from an electric field that exceeds the rate of energy loss from interactions with air, lays the ground work for TGF theory. Figure 1.4 shows a plot describing the relationship between the effective frictional force vs kinetic energy of an electron in air. The horizontal line eE is the force associated with a net electric field E, while the curve represents the opposing 'frictional' force on the electron. You can see that electrons with energies greater then ε_{th} will "run away" to greater and greater energies as the 'frictional force' is at a minimum at relativistic electron energies. When the electric field is increased above the critical field, E_c , then all free electrons, particularly the thermal population at low energies may run away. This mechanism is usually called "cold runaway" or "thermal runaway," [Gurevich, 1961]. The E_c field amplitude has been inferred to be between 200-300kV/cm from laboratory spark experiments [Celestin and Pasko, 2015] which is within the limits of the electric fields at the very tips of lightning leaders.

The runaway electrons described by Wilson, with the addition of Møller scattering or 'hard' collisions, will undergo an exponential multiplication dependent on the length L of the electric field region and the mean free path λ of the electron,

$$N = N_0 e^{L/\lambda} \tag{1.1}$$

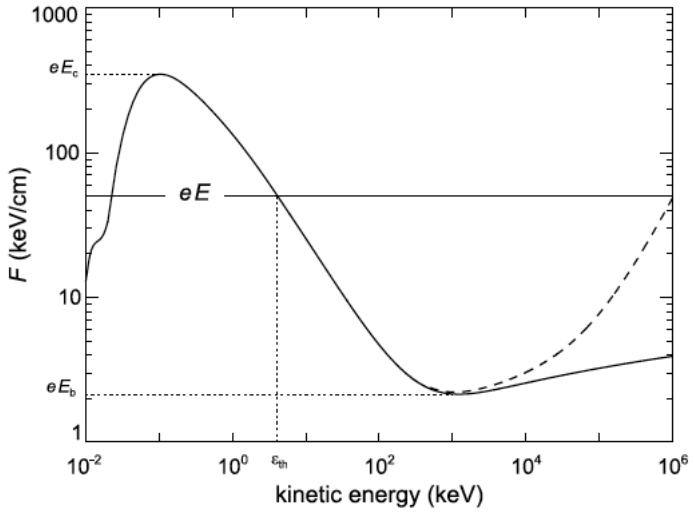

Figure 1.4: The effective frictional force experienced by a free electron (or positron) moving through air at STP as a function of kinetic energy. The solid curve is due to inelastic scattering of the electron by air molecules, and the dashed curve indicates the effects of bremsstrahlung emission. The horizontal line shows the electric force from a 50 kV/cm electric field. Runaway electrons occur for kinetic energies greater than the threshold energy, $\varepsilon > \varepsilon_{th}$. In the figure, E_c is the critical electric field strength for which low-energy thermal electrons will run away, and E_b is the break-even field. Source: [Dwyer, Smith, and Cummer, 2012]

resulting in an increasing number of relativistic runaway electrons for each energetic seed electron injected into the high-field region as long as the electric field amplitude exceeds a certain threshold [Gurevich et al., 1992, 2001]. This threshold has been found to be slightly above the break even field at $E_{RREA} = 2.84$ kV/cm at sea level [Dwyer 2003], in agreement with the value 2.83 kV/cm by Babich et al 2004. This relativistic runaway electron avalanche (RREA) process is a signature characteristic of the TGF energy spectrum. Dwyer et al. (2012) analytically derived the RREA energy spectrum from the model of exponential growth of the relativistic electron fluence in the previous

equation (1.1) by integrating the mean free path over the length of the avalanche region,

$$\frac{L}{\lambda} = \int_0^L \frac{dz}{\lambda} \tag{1.2}$$

where the mean free path or e-folding length may be written approximately as,

$$\lambda = \frac{7.3MeV}{eE - F_d} \tag{1.3}$$

with eE-F_d being the net force and the resulting energy E is expressed by equation (1.4).

$$E = z(eE - F_d) \tag{1.4}$$

The integral of equation (1.2) is re-written and solved in terms of E, with bounds z to z+dz and substituted into the equation of fluence (1.1) to give the number of electrons per unit energy (1.5).

$$f_e = \frac{N}{7.3MeV} e^{-E/7.3MeV} \tag{1.5}$$

The difference between the energy spectrum of bremsstrahlung emission from an electron with kinetic energy E, can be approximated by a power law with index -1, i.e. $1/E_p$, up to the energy E. The convolution of $1/E_p$ with the electron spectrum will give a good approximation of the photon spectrum for a TGF.

$$f_p = \frac{N_p}{E_p} e^{-E_p/7.3MeV} \tag{1.6}$$

Figure 1.5 illustrates a side by side comparison of this RREA model gamma ray spectrum next to a well resolved TGF energy spectrum using a catalog of observational data from the Reuven Ramaty High Energy Solar Spectroscopic Imager satellite (RHESSI).

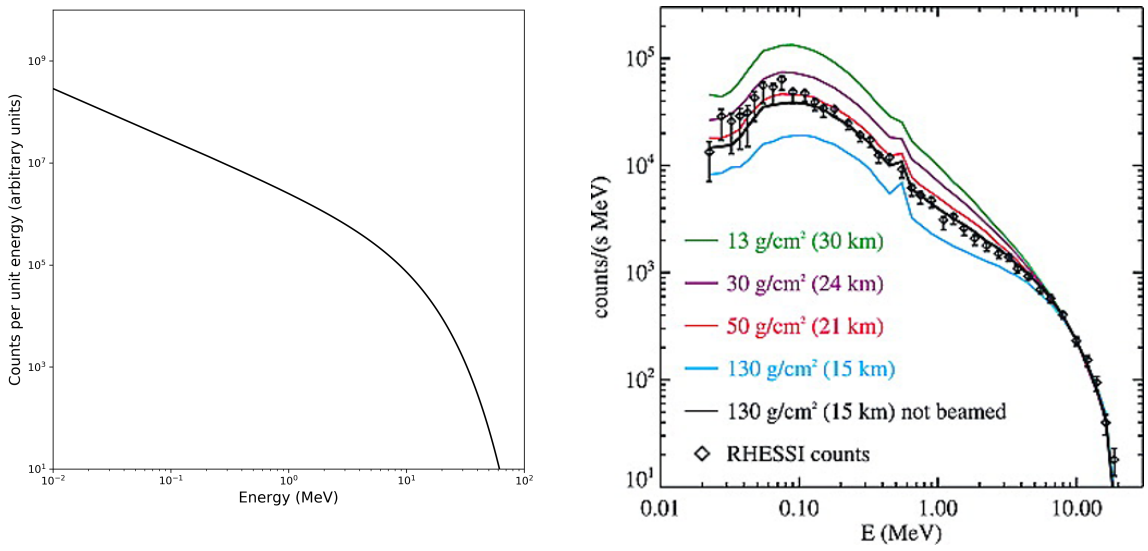

Figure 1.5: Left: Analytical model of the RREA energy spectrum. Characterized by a power law with index -1 and a steep exponential decay. Right: The first well resolved energy spectrum of TGFs using a large library of TGF observations from the Reuven Ramaty High Energy Solar Spectroscopic Imager (RHESSI). The RHESSI data points are compared to TGF model spectra (colored curves) that have been simulated as having originated at different altitudes in the atmosphere. This showed that TGFs were occurring at thunderstorm altitudes (15-21 km). Source: Dwyer and Smith 2005

The RREA mechanism, given a 'seed' electron of energy greater then ε_{th}, results in the significant multiplication of high energy electrons and thus generating high energy radiation through bremsstrahlung interactions with atmospheric molecules. However, a difficulty is that the known fluence of gamma radiation from TGF events detected by spacecraft imply an energetic electron population that far exceeds the limits of multiplication of cosmic ray 'seed' electrons under RREA multiplication. The estimated amount of multiplication, up to 10^6 electrons, falls short of what is actually

observed.

1.2.1 Relativistic Feedback

In 2003 Joseph Dwyer published a runaway electron production mechanism that relies on a feedback effect from positrons and back scattered energetic photons [Dwyer, 2003]. Figure 1.6 illustrates the multiplication mechanisms starting with Wilson's runaway electron, adding the physics of RREA avalanches and the emission of bremsstrahlung photons, a fraction of which will either Compton back-scatter or pair-produce in air. Some of the back-scattered photons propagate to the start of the avalanche region and produce other runaway electrons resulting in a secondary avalanche. Additionally, the positrons created by pair-production can turn around, if created in the avalanche region, and run away in the opposite direction of the electrons. These positrons propagate to the start of the avalanche region and can produce additional runaway electrons by hard elastic scattering with atomic electrons in the air. The result of this positive feedback is that the number of runaway electron avalanches increases exponentially,

$$N = N_0 e^{L/\lambda} \gamma^{t/\tau} \tag{1.7}$$

on a timescale measured in microseconds [Dwyer 2003, Babich et al. 2005]. The factor γ is a fractional increase in the number of runaway electrons during each feedback cycle of duration τ. This model can account for the large fluences and times scales of observed TGFs [Dwyer 2008].

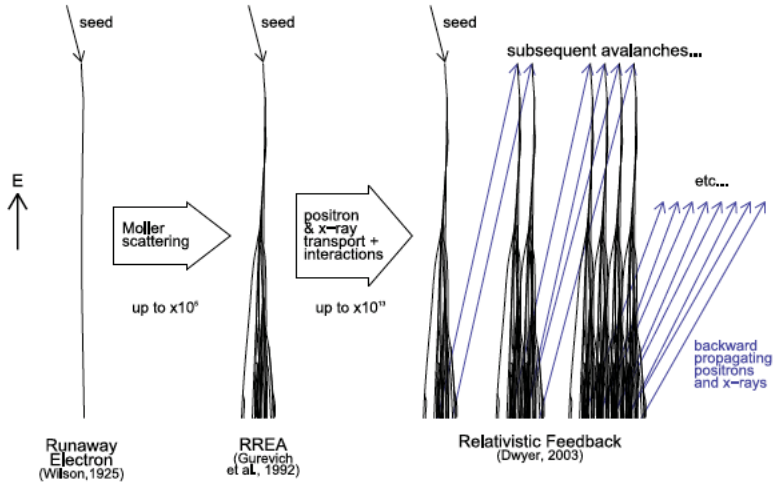

Figure 1.6: Schematic diagram summarizing the three mechanisms for generating energetic electrons in an atmosphere. By including Møller scattering in the runaway electron mechanism, a relativistic runaway electron avalanche (RREA) is produced, with an increase in the number of runaway electrons over the Wilson runaway electron mechanism. By including positron and x-ray transport and interactions to the RREA mechanism, Relativistic Feedback is produced, with an increase in the number of runaway electrons over the RREA mechanism. The energetic seed particle that becomes the first runaway electron may be supplied by atmospheric cosmic-rays, radioactive decays or by thermal runaway electron production during lightning or other sparks. Source: [Dwyer et al. 2012]

1.2.2 Thermal Runaway Mechanism

Relativistic feedback is one of three models that seeks to explain observed TGF luminosity. The feedback model uses a relatively uniform electric field with large volume and amplitudes approaching the upper limits of ambient background electric field measurements. The other two models, described by a thermal runaway process, rely on electric field enhancements near lightning leader/streamer tips to provide a substantial enough population of seed electrons to achieve observed luminosities. In the first of these two models moderately energetic seed electrons created via 'cold runaway' close to the leader tip undergo RREA in the large-scale ambient field of the storm [Dwyer 2008, Moss et al. 2006]. The second thermal runaway model does not rely on a large

scale field at all. Runaway electrons emitted from negative streamers are shown, in the model (Figure 1.7), to be sufficient when combined with 'cold runaway' at the leader tip and RREA in a limited volume to obtain a flux of energetic electrons consistent with the typical number of electrons involved in TGF production [Moss et al. 2006, Carlson et al. 2010, Celestin & Pasko 2011].

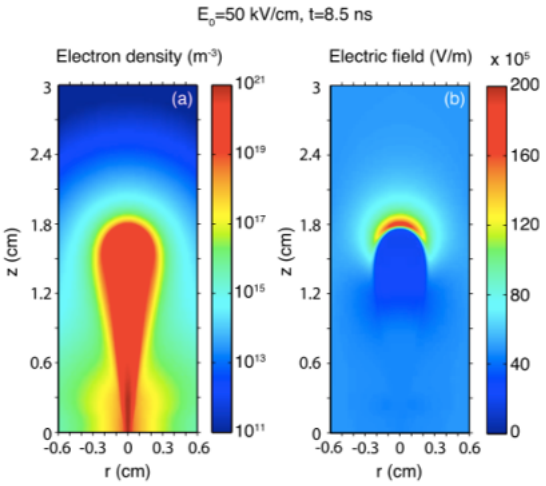

Figure 1.7: Cross-sectional views of (a) electron density and (b) electric field in a negative streamer simulated in air at ground pressure for a homogeneous applied electric field of 50 kV/cm. Source: [Celestin & Pasko 2011]

Of these two thermal models neither can be definitively ruled out. There have been some papers e.g. Xu, Celestin & Pasko (2012) that have tried to model TGFs with extended cold runaway spectra (the second of the two mentioned thermal models) with results not out of the realm of possibility. The bremsstrahlung mechanism has a tendency to destroy information about the source electron spectrum so there tends to be a lot of wiggle room. But, with the latter model having such a relatively small electric field volume, pair production by gamma rays would occur largely outside the avalanche region in which positrons could run away. This would suppress any reverse

bremsstrahlung beam. Recent publications of reverse beam TGFs would suggest that the electric field volume is sufficiently large to account for these observations [Bowers et al. 2018, Pu et al. 2020]. A thermal runaway model that incorporates an RREA process in a large scale field is more plausible, considering the reverse beam observations, but if it were the only physics involved the expected time profile of a TGF would be characterized by the 'stepping' nature of lightning leader electric field enhancements, i.e. you would expect to see either very short $<10\mu$s TGFs or a series of short time scale discreet packets of gamma ray emission over 10-100s of microseconds. Something along these lines has been observed in one location in Utah [Abassi 2018] but a larger set of TGF observations [Foley et al. 2014; Hare et al. 2016; Colalillo et al. 2021] suggest a smoothly distributed time profile with typical duration's in the 10s to 100s of microseconds, implying either no reliance on multiple lightning leader electric field enhancements or additional physics that serves to smooth out the time profile.

There is no clear observation to suggest thermal runaway over relativistic feedback. But most observed TGFs have a direct temporal association to a lightning event suggesting the eletrodynamics of the lightning leader plays an important role. It is likely the TGF mechanism requires a combination of physics. Lightning leader electric fields to kick start the process by generating a population of high energy 'seed' electrons via 'cold runaway'. A larger scale ambient background field above the RREA threshold which results in avalanche growth of the aformentioned high energy electrons. And finally, relativistic feedback which both increases the luminosity and possibly smooths

out the time profile of what might otherwise be several discrete bursts of gamma rays. How big of a role each of these physical processes play in the overall TGF mechanism is unknown at this time.

1.2.3 Positrons, Neutrons and the Reverse Beam

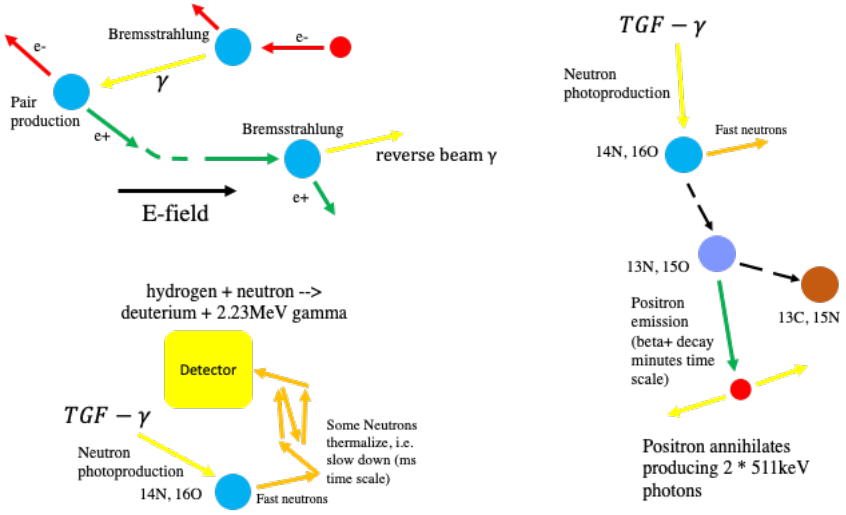

Figure 1.8: Top left: Qualitative description of the source of 'reverse beam' gamma rays of a TGF. High energy bremsstrahlung gammas from electrons can pair produce in the electric field resulting in a high energy positron running away in the opposite direction and creating a 'reverse' gamma via a bremsstrahlung interaction. Bottom left: Description of detector response to thermalized photo-neutrons created via gamma photon interactions with atmospheric nuclei. Right: The process of radioactive decay from unstable isotopes of oxygen and nitrogen and the resulting emission of positrons and subsequent 511keV annihilation photons.

Regardless of whether the feedback mechanism proves to be significant in the TGF process the physics of pair production remains. If you have gamma rays above roughly 1 MeV, moving through atmospheric nuclei, a portion will pair produce a relativistic positron. If that relativistic positron is created within the electric field responsible for the TGF production it too will run away and produce gamma rays via bremsstrahlung in the opposite direction to the main TGF emission. This reverse beam

TGF has been observed via an airborne observation [Bowers et al. 2018] and surprisingly an orbital observation by Fermi [Pu et al. 2020] to be discussed in detail in section 2. The reverse beam will be dimmer as the positrons can not avalanche like the electrons. As a consequence a much great percentage of positrons will be subject to most of the potential drop, resulting in a harder spectrum (larger high energy : low energy photon ratio) that will be more narrowly beamed. [Bowers et al. 2018, Ortberg et al. 2020].

Photo-neutrons can also be created from the TGF gamma interacting with nuclei. From the creation of a photo-neutron by a gamma photon two processes can result. First the ejected neutrons can thermalize as they precipitate to the ground on time scales of milliseconds to several hundred milliseconds. When thermalized neutrons interact in detector material or nearby materials a neutron capture process can occur resulting in the emission of a photon. Bowers et al. (2017) observed the first neutron signature of a TGF using a plastic detector, i.e., hydrogen, which when it captures a neutron forms deuterium in an excited state. There is an immediate relaxation to a ground state producing a gamma photon in the detector material of 2.2 MeV.

The second process picks up just after the neutron has been ejected. The resulting unstable isotopes of nitrogen and oxygen will undergo beta-decay, emitting positrons on a time scale of minutes. These positrons will quickly annihilate with free electrons emitting two characteristic 511 keV X-rays. Enoto et al. (2017) were able to detect this positron annihilation line with very good agreement to the decay time signature of 13N

and 15O as the cloud of radioactive atmosphere passed over head of their sensors.

1.3 Satellite Data and Geographic Distributions

The Reuven Ramaty High Energy Spectroscopic Imager (RHESSI) satellite was launched in 2002 into a 580 km 38^o inclination orbit. It contained an array of nine high-resolution germanium detectors with an energy range of 3 keV to 20 MeV [Smith et al. 2002]. The large number of RHESSI events (relative to previous BATSE detections) allowed for a detailed comparison of the geographical distribution of TGFs with other meteorological phenomena. Figure 1.9 (top) shows the global distribution of TGFs detected by the RHESSI satellite between 2002 and 2015 [Grefenstette et al. 2009].

The Fermi Gamma-ray Burst Monitor (GBM) instrument, launched in 2008 with an orbital inclination of 25.7^o, consists of 12 uncollimated NaI scintillators pointing in different directions and two large bismuth germanate (BGO) scintillators. The NaI scintillators primarily detect photons up to 1 MeV, while the BGO scintillators operate up to 40 MeV. Figure 1.9 (bottom) shows the global distribution of TGFs detected by the Fermi satellite between 2008 and 2016 [Gruber 2014; Kienlin 2014; Bhat 2016].

Studies comparing the TGF distribution with the global occurrence of lightning found deficits of TGFs at high latitude. One proposed explanation for this is that the altitude at which TGFs occur may be higher in the tropics, where the tropopause and subsequently thunderstorm altitudes are higher. Because gamma-rays more easily

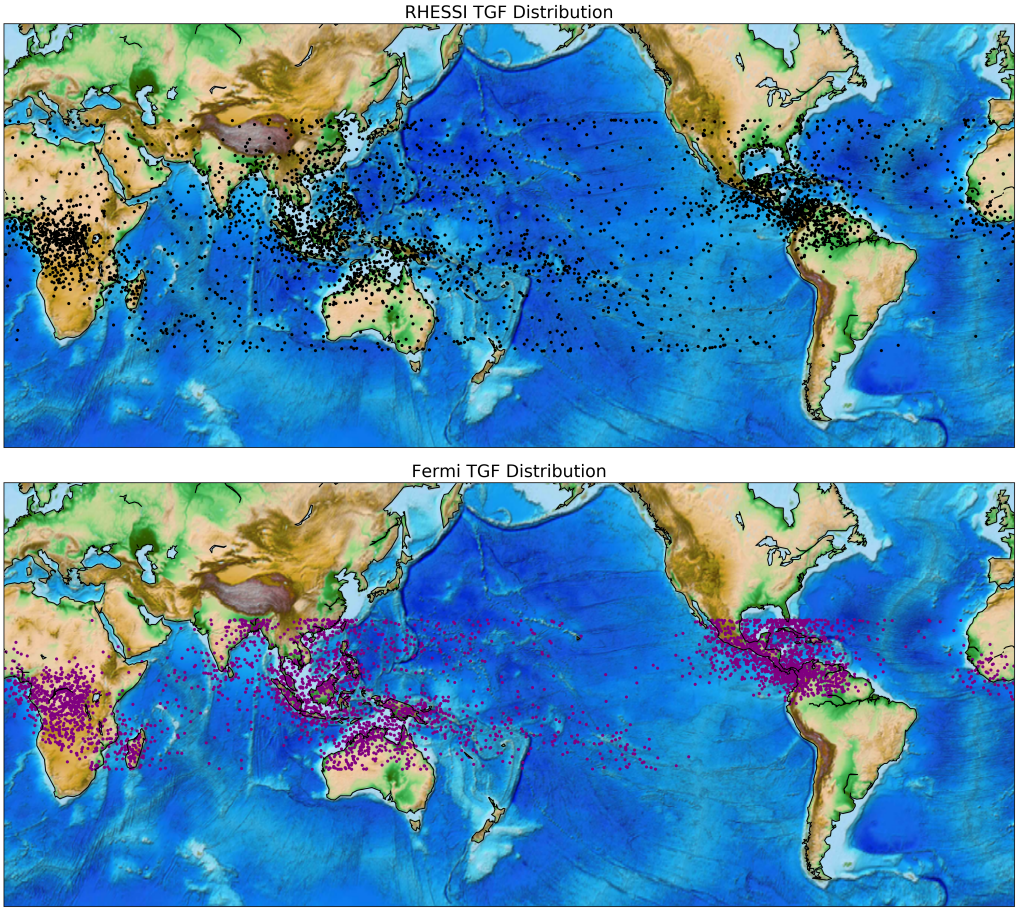

Figure 1.9: Top: Global distribution of TGFs (black data points) detected by the RHESSI satellite between 2002 and 2015. Bottom: Global distribution of TGFs (purple data points) detected by the Fermi satellite between 2008 and 2016

escape into space at higher altitude, TGFs would be more frequently detected in the tropics [Williams et al. 2006]. A further study [Smith et al. 2010] compared the RHESSI TGF map with the map of lightning produced by NASA's Lightning Image Sensor and Optical Transient Detector instruments. It was found that the altitude effect was not as strong as originally thought, with the attenuation in the total number of gammas having an e−folding depth of 45 g/cm^2 of overlying atmosphere. The prevalence of TGFs in the tropics likely has a more complicated explanation than simply gamma-ray

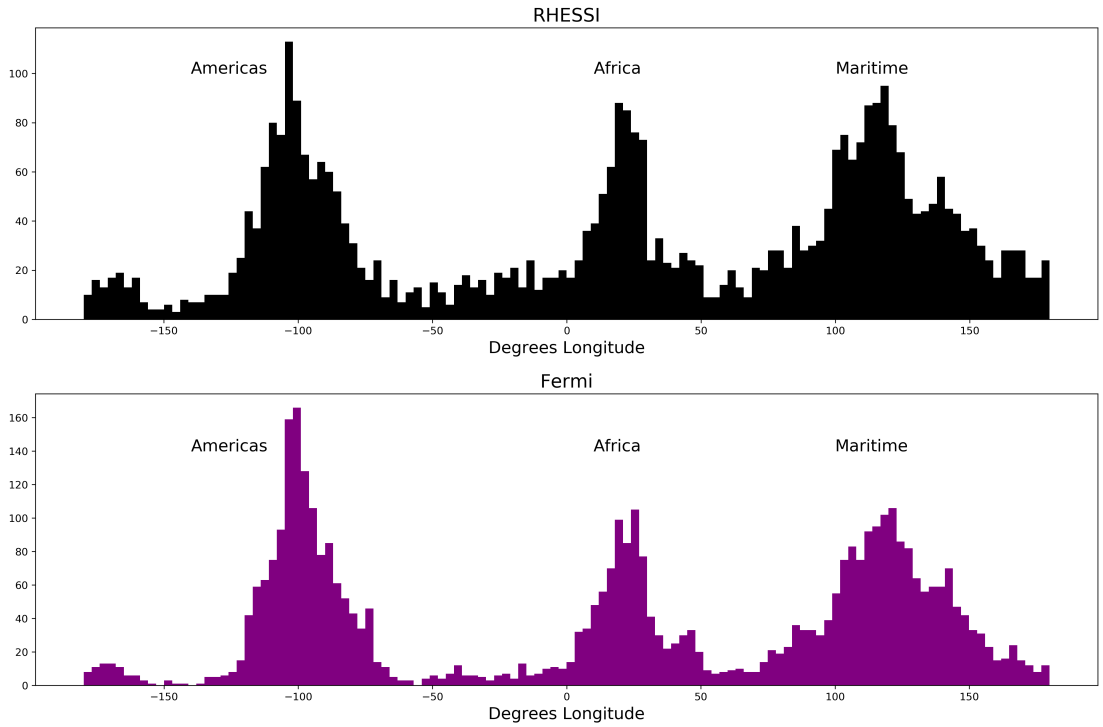

Figure 1.10: Top: Longitudinal distribution of TGFs observed by the RHESSI satellite between 2002 and 2015. Botton: Longitudinal distribution of TGFs observed by the Fermi satellite between 2008 and 2016

escape. Further anomalies, such as a lower TGF/lightning ratio in Africa relative to the Americas, and a shift in longitude between the peaks of lightning and TGFs within the Maritime Continent suggest that a significant part of the difference between lightning and TGF distributions may lie in meteorological conditions that favor the production of TGFs, not just their escape into space. Another observation and study of RHESSI data [Hazelton 2009] found that the TGF/lightning ratio was higher for coastal regions than for inland or oceanic regions.

For a more quantitative look at the global distribution of TGFs of each satellite, figures 1.10 and 1.11 plot longitudinal and latitudinal distributions respectively. The

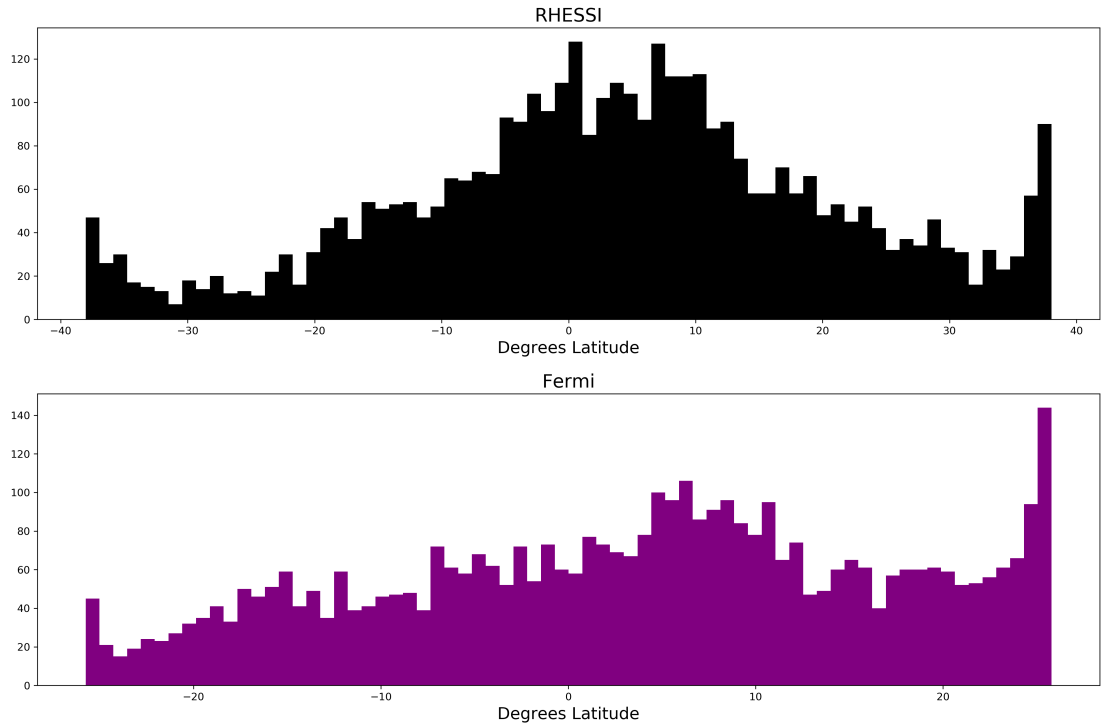

Figure 1.11: Top: Latitudinal distribution of TGFs observed by the RHESSI satellite between 2002 and 2015. Botton: Latitudinal distribution of TGFs observed by the Fermi satellite between 2008 and 2016

longitudinal distributions show the TGF preference for continental land masses. You can clearly see the effect orbital inclination has on the maximum and minimum latitudes each satellite traverses. There is also a noticeable skew for larger TGF event rates for the northern hemisphere in both the FERMI and RHESSI latitude histograms. Explanations for this skewing may include lower latitude event rates being suppressed by the South Atlantic Anomaly, and more land mass in the northern hemisphere. In general more land equals more lightning, but also TGFs tend to be more coastal with the implication that more land equals more coastline, thus higher TGF rates.

1.4 Lightning Detection and Radio Sferics

The study of TGFs in many respects is inseparable from the studying of lightning. Lightning detection is used to associate TGFs with individual lightning flashes, assist in determining TGF source locations, give insight into the temporal relationship between lightning leader processes and TGF mechanisms, and also constrain altitude estimates as we will see in the following paper. It is important to understand how lightning is detected and what we can learn from its electromagnetic emissions.

As a result of the scale of lightning (km's in length) and the extreme currents (up to 100s of kiloamperes) lightning behaves like a very large and powerful antenna. The large current amplitude processes that propagate along the large scale existing leader channels of lightning produce electromagnetic energy over a wide bandwidth with the bulk of the energy radiated in frequencies <30 kHz, the very low frequency (VLF) band. Just like with AM radio signals and ham radio frequencies, these VLF signals are able to travel 1000s of kilometers due to low attenuation travel within the Earth-Ionosphere waveguide [Rakov and Uman, 2003].

Figure 1.12 shows a diagram of the signal propagation paths between a lightning event and a radio receiver. The propagation paths of the VLF signal from the mostly vertical 'antenna' of the lightning leader channel can be classified as either ground or sky wave. Ground waves exist only for vertical polarization, produced by

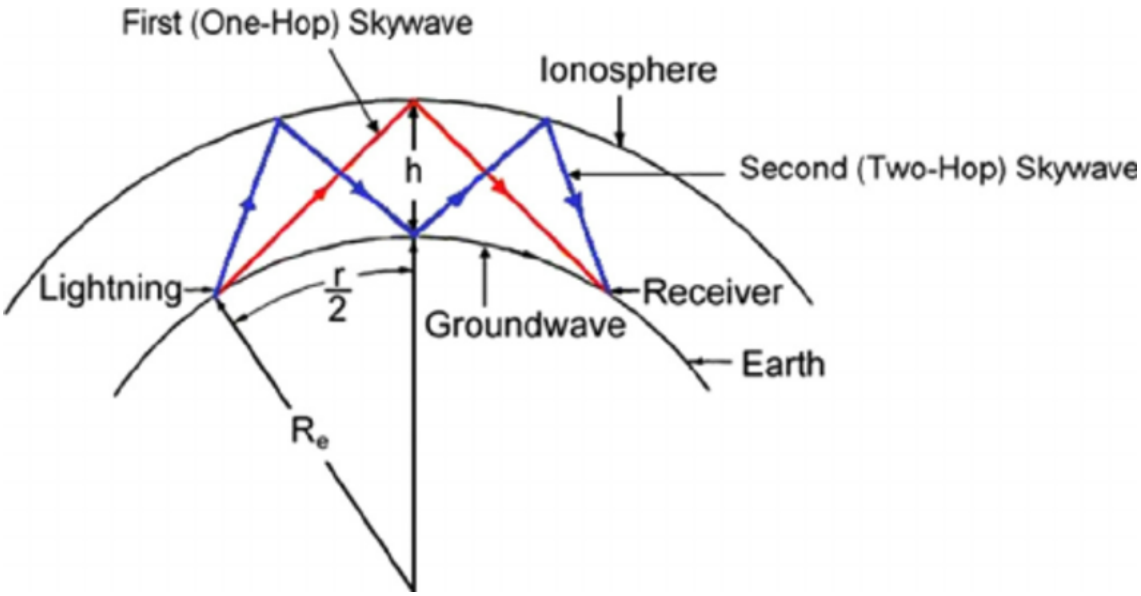

Figure 1.12: Diagram of signal propagation paths between a lightning event and a distant radio receiver. The radio waves will propagate in two paths, either as a ground wave along the conductive Earths surface or as a reflected wave or sky wave in the Earth-Ionosphere waveguide. [Somu et al. 2015]

vertical antennas. The radio signal spreads out from the leader channel along the surface of the Earth. Instead of just travelling in a straight line the radio waves tend to follow Earth's curvature. This is because currents are induced in the ground and this action slows down the wave-front in the region, causing it to tilt downwards. With it tilted in this direction it is able to curve around the Earth and be received beyond the horizon, albeit with increasing attenuation due to the energy losses with the conductive Earth. The sky wave by contrast can travel great distances with little attenuation. The VLF signal is reflected between the lower layer of the ionosphere and the conductive Earth just like light through a waveguide.

Understanding each of these components is important to interpreting the radio sferic of

the VLF signal at the receiver. At shorter distances (less than a couple hundred km's) the ground wave dominates. The path length of the ground wave is shorter and hence will be received earlier than the sky wave. As the distance between the VLF source and the receiver increases the ground wave is attenuated and the sky wave begins to dominate. Additionally, with increasing distance the ground wave path length (curvature of the earth) increases at a greater rate than the reflected sky wave. This results in the time difference between the ground and sky wave arrival time at the receiver decreasing, with the signals eventually combining and finally only the sky wave being observed with the ground wave unable to propagate from energy losses.

Global networks of VLF sensors such as the World Wide Lightning Location Network (WWLLN) and Earth Networks Total Lightning Network (ENTLN) take advantage of this long distance radio propagation to detect lightning flashes with extremely good timing (μs precision using GPS receivers), location (within a few km), and polarity. Advanced lightning location networks can employ either magnetic or electric field sensors to detect lightning radio waves. Magnetic direction finding (MDF) uses orthogonal loop antennae to measure the magnetic flux of the lightning induced radio waves. A loop antenna, as shown in the top image of Figure 1.13, is used to take advantage of Faraday's law that states the voltage across the open ends of the loop will be equal to the time rate of change of the flux through the loop. The flux is determined by the angle θ with respect to the normal vector of the plane of the loop.

As long as a general location of the source current is known (cardinal direction)

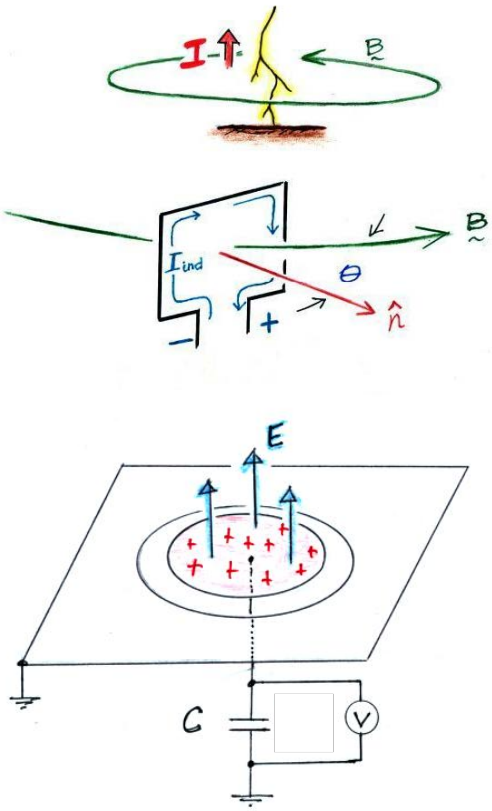

Figure 1.13: Top: Sensor in a magnetic direction finder system uses two orthogonal loop antennas. One loop is shown. A distant lightning strike produces a horizontal magnetic field, B, that passes through the antenna. Faraday's law states that the voltage V across the open ends of the loop antenna is equal to -Acosθ $\frac{dB}{dt}$. The output signal from the antenna will depend on the location of the lightning strike with respect to the plane of the antenna (the cosθ term). Bottom: Depiction of a 'flat plate antenna' electric field sensor. A time varying electric field causes current to flow to and from the center sensor plate. The voltage measured across the capacitor from the electric field induced current in the plate is equal to $\frac{\epsilon_0 AE}{C}$. Image source: Lectures on Atmospheric Electricity given by Philip Krider at the University of Arizona.

with respect to the antenna then a positive or negative flux measurement will indicate the source current direction (up or down) of the lightning event. Using two loops that are orthogonal two each other allows for a more precise estimate of the direction of the current source as each one contributes to the direction vector.

With multiple MDF sensors spaced over many kilometers the direction vectors can be triangulated to provide a location estimate of the source current. That combined with using a time of arrival (TOA) method, where the arrival time differences at each sensor are used to determine a source location, a high degree of accuracy can be obtained for determining individual flash locations.

To measure the electric field component of the lighting radio pulse a version of a 'flat plate antenna' is used. As a time varying electric field causes current to flow to and from a conductive sensor plate, voltage is measured across the sensing element and ground. Additional capacitive circuit elements are added between the output of the sensing element and ground to allow for faster or slower time constants, changing the frequency response of the instrument. A depiction of a 'flat plate' electric field sensor is shown in the bottom image of Figure 1.13. An array of these sensors, spaced over 100s of km's and using TOA techniques, can provide a high degree of accuracy in determining lightning locations.

Along with deriving location and timing information, both magnetic and electric field sensors, record the radio wave sferic data which makes it possible to see individual current pulses of the lightning leader progression. Since the suspected correlation between TGFs and lightning [Cohen et al., 2006; Cummer et al., 2005; Stanley et al., 2006] was confirmed using VLF radio signals and TGF observations from both RHESSI and Fermi-GBM [Connaughton, 2010; Collier et al., 2011] a great amount of effort has gone

into determining if there is a consistent temporal relationship between the lightning leader progression and the TGF mechanism [Lu et al., 2011; Marshall et al., 2013; Gjesteland et al., 2017; Lindanger et al. 2022]. This multi-wavelength approach to TGF observations has led to the discovery of unique radio sferic characteristics that appear to be the result of the current induced by the TGF itself, or more precisely the large population of relativistic electrons responsible for the TGF [Cummer et al.,2011; Lu et al.,2011; Dwyer and Cummer, 2013; Lyu et al.,2016; Cummer et al.,2017; Pu et al.,2019]. The following two papers, intended for publication, focus on these multiwavelength observations and give a detailed explanation of the radio sferic data attributed to TGF currents.

Section 2

Fermi Reverse Beam TGF

Determining a Lower Limit of Luminosity for the first Satellite Detected Reverse Beam Terrestrial Gamma-ray Flash Produced by a Cloud-to-Ground Lightning Leader

Jeffrey M. Chaffin, Yunjiao Pu, David M. Smith,

Steve Cummer, Michael Splitt

2.1 Abstract

We provide an updated analysis of the gamma-ray signature of a terrestrial gamma ray flash (TGF) detected by the Fermi Gamma-ray Burst Monitor first reported by Pu et al. (2020). A TGF produced 3 ms prior to a negative cloud-to-ground return stroke was close to simultaneous with an isolated low frequency radio pulse during the leader's propagation, with a polarity indicating downward moving negative charge. In prior observations this 'slow' low frequency signal has been strongly correlated with

upward (opposite polarity) directed TGF events [Pu et al., 2019; Cummer et al., 2011] leading the authors to conclude that the Fermi gamma ray observation is actually the result of a reverse positron beam generating upward directed gamma rays. We investigate the feasibility of this scenario and determine a lower limit on the luminosity of the downward TGF from the perspective of gamma-ray timing uncertainties, TGF Monte Carlo simulations, and meteorological analysis of a model storm cell and its possible charge structure altitudes. We determined the most likely source altitude of the reverse beam TGF to be 7.5 km $\pm$ 2.6 km, just below an estimated negative charge center at 8 km. At that altitude the Monte Carlo simulations indicate a lower luminosity limit of $2{\times}10^{18}$ above 1 MeV photons for the main downward beam of the TGF making the reverse beam detectable by the Fermi Gamma Ray Burst Monitor.

2.2 Introduction

It is widely accepted that Terrestrial Gamma Ray Flashes (TGFs) are the result of bremsstrahlung interactions of highly energetic electrons undergoing avalanche growth. This exponential growth of relativistic electrons is driven by thunderstorm electric field activity consisting of the background field strength of the storm cell and enhancements to that field by the transient fields associated with lightning leaders [Dwyer et al., 2012]. But since the first observations of TGFs [Fishman et al., 1994] the question of source altitude and therefore intrinsic brightness has proven difficult to answer. It was initially proposed that the source altitude of TGFs must be high in the stratosphere

connected with the runaway breakdown of Sprites [Taranenko and Roussel-Dupré, 1996]. Later, the analysis of the cumulative energy spectra of TGFs observed by the Reuven Ramaty High Energy Solar Spectroscopic Imager (RHESSI) lowered the source altitude estimate by at least 30 km. Using the Relativistic Runaway Electron Avalanche (RREA) model [Gurevich et al., 1992; Dwyer, 2003] it was shown that the production altitudes of the RHESSI TGF observations were consistent with 15-21 km, conventional thunderstorm altitudes, and with intrinsic brightness estimates as high as 10^{17} gammas above 1 MeV [Dwyer and Smith, 2005]. This analysis, along with work linking TGFs to the lightning discharge process [Cummer et al., 2005; Stanley et al., 2006] confirmed that TGFs occur lower in the Earths atmosphere and at intensities much brighter than previously considered.

Just in the last few years we have seen that TGFs can occur at any altitude where thunderstorm charging and lightning initiation take place. This has been observed with numerous ground-based observations of downward directed TGFs at altitudes as low as 1-2km and with intrinsic brightness comparable to those seen from space [Dwyer et al., 2003; Tran et al., 2015; Hare et al., 2016; Bowers et al., 2017; Enoto et al., 2017; Colalillo, 2017; Smith et al., 2018; Abbasi et al., 2022; Wada et al., 2022].

Typically observations of downward vs upward TGFs are categorized by ground vs orbital observations respectively. However, this does not rule out the possibility of TGF detection when observed from the opposite view point, e.g. detecting an upward di-

rected TGF from the ground. High energy gamma rays can generate positrons through pair production; and if produced while still within the avalanche region will run away in the opposite direction of the electrons [Gurevich et al., 2000]. The runaway positrons, though smaller in number and not being able to avalanche like their electron counterparts, will still produce their own gamma rays via bremsstrahlung [Dwyer, 2003]. This reverse beam component of the TGF has previously been observed by the Airborne Detector for Energetic Lightning Emissions (ADELE) when flying through the eye-wall of Hurricane Patricia aboard the National Oceanic and Atmospheric Administration's Hurricane Hunter WP-3D Orion [Bowers et al., 2018]. Modeling work by Ortberg et al. (2020) suggests that upward TGFs observable from space can theoretically be co-observed from the ground if the ground observation point is at sufficient altitude, say a mountaintop.

But what about detecting a downward TGF from orbit? Pu et al. (2020) published a Fermi TGF that is unambiguously associated with a negative CG lightning flash, i.e. a lightning leader with a polarity that would move negative charge towards the ground. They arrived at this conclusion using observational data from the Fermi Gamma-ray Burst Monitor (GBM) and simultaneous ground-based radio measurements of lightning from a network of very low frequency (VLF) and low frequency (LF) magnetic sensors run by Duke University.

Research done in the last decade has shown a relationship between TGFs and sev-

eral types of low frequency radio emissions from lightning [Cummer et al., 2011; Lyu et al., 2015; Lyu et al., 2016; Pu et al., 2019; Lyu et al., 2021]. Of these unique radio pulses simultaneous to TGF production the 'slow pulse' [Cummer et al. 2011] is characterized by a distinct slow temporal signature (50-100 μs). The pulse comes in the midst of initial breakdown pulses (IBPs) which are each typically less then 10 μs in duration. Dwyer and Cummer (2013) demonstrated how this slow pulse is predicted by the feedback TGF model and can be interpreted as an observable current moment of the TGF electron avalanche process itself. The Fermi TGF in question [Pu et al., 2020] was simultaneous to a distinct slow pulse (120 μs) that is consistent with the slow low frequency pulses that have previously been associated with TGFs produced by IC leaders [Cummer et al., 2011; Ostgaard et al. 2013; Pu et al., 2019]. The authors make clear that the polarity of this slow pulse is opposite to that for upward TGFs produced by IC leaders and is the same as that for a downward TGF produced by a rocket-triggered upward positive leader [Hare et al., 2016]. The conclusion drawn is the TGF must be directed downwards and the Fermi observation is consequently of the reverse beam (positron initiated) gamma-rays.

Using a timing alignment procedure detailed in Pu et al. (2019) and location data from the National Lightning Detection Network (NLDN), Pu et al. (2020) determined a source altitude for the TGF to be from 5.4-6.7 km. The slow pulse event occurs roughly 3 ms after the initial breakdown pulses signaling the initiation of the downward negative leader, and roughly 3 ms prior to the ground contact return stroke. Assuming

a leader propagation speed of 10^6 m/s [Zhu et al., 2016] this puts the initiation altitude of the leader nominally at 6km leading the authors to argue a scenario where the TGF was produced ahead of the positive polarity end of a possible bidirectional CG leader.

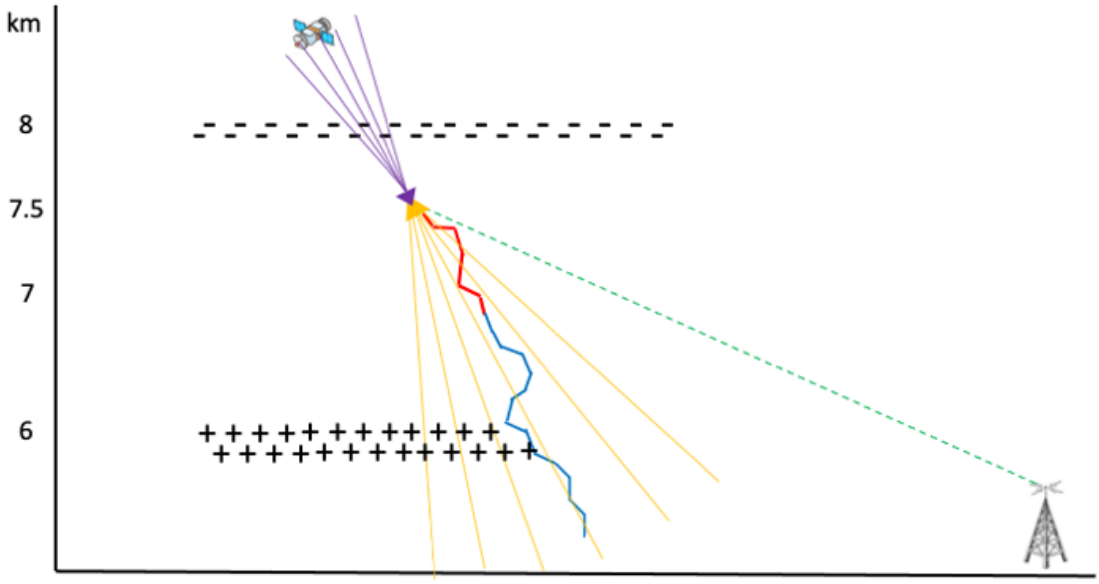

Figure 2.1: Qualitative depiction of the proposed TGF scenario. Actual altitude values are determined by the methods in sections 4 and 5. Model storm cell analysis estimates a negative charge center at 8 km and positive charge center at 6 km. A bi-directional CG leader initiates at roughly 6-7 km. The negative polarity leader (blue) propagates towards ground resulting in a return stroke 6ms later. The positive polarity end of the leader (red) propagates upward initiating a downward TGF 3ms after leader initiation at roughly 7.5 km, just below the negative charge center. The resulting TGF beaming angle is such that the reverse beam is closely aligned (within a 50km annulus) with the Fermi/GBM satellite. Fermi/GBM observes a small count rate TGF (purple) simultaneous to the resulting radio sferic observation (green) created by the current moment associated with the electron avalanche (RREA) responsible for the TGF.

Considering that a TGF would experience considerable absorption from a source altitude of 6 km, and that the reverse beam TGF is understood to be roughly 1% the brightness of the main forward beam [Ortberg et al., 2020] is this observation under these circumstances possible? Can a reverse beam TGF be seen from space from

so deep in the atmosphere and how bright would the main (downward) TGF need to be? In this paper we use Monte Carlo simulations to estimate the brightness required for a reverse beam TGF to be observed at orbital altitudes. We will attempt to further constrain the likely source altitude using a charge structure analysis of the storm cell and provide a new source altitude estimate with updated timing alignment analysis.

2.3 REAM Monte Carlo Simulations

To determine a lower limit of TGF luminosity we performed several Monte Carlo simulations using GEANT4 [Agostinelli et al., 2003; Allison et al., 2006, 2016]. Assuming a RREA production mechanism we compared the number of photons incident on both Fermi/GBM bismuth germanate (BGO) detectors, as published in Pu et al. (2020), to simulated gamma ray fluence from the reverse beam component of a downward directed TGF. We ran simulations for various altitudes and scaled for a range of intrinsic brightness. In each simulation, gamma rays with energy, z-component of position and angular distribution information were released and propagated upward through a mass model of the atmosphere derived using values from the U.S. Standard Atmosphere (1976). The resulting radiation field produced at an orbital altitude of 530km was captured.

The input photon distribution comes from simulations of TGFs using the Relativistic Electron Avalanche Model (REAM) discussed in Dwyer (2003, 2007) and Dwyer and

Smith (2005). Seed electrons greater than 1MeV are injected into a high field region of -400 kV/m resulting in an exponentially increasing relativistic electron population. The energy distribution of the electrons can be approximated by the exponential $e^{-E/7.3MeV}$ [Dwyer et al. 2012]. The subsequent bremsstrahlung gamma rays from electron and positron interactions with atmospheric molecules are tracked and recorded with energy, position, and direction information. Photons with z-component momentum aligned with the electric field direction, i.e. the reverse beam, are used as the input in the previously mentioned atmospheric simulation.

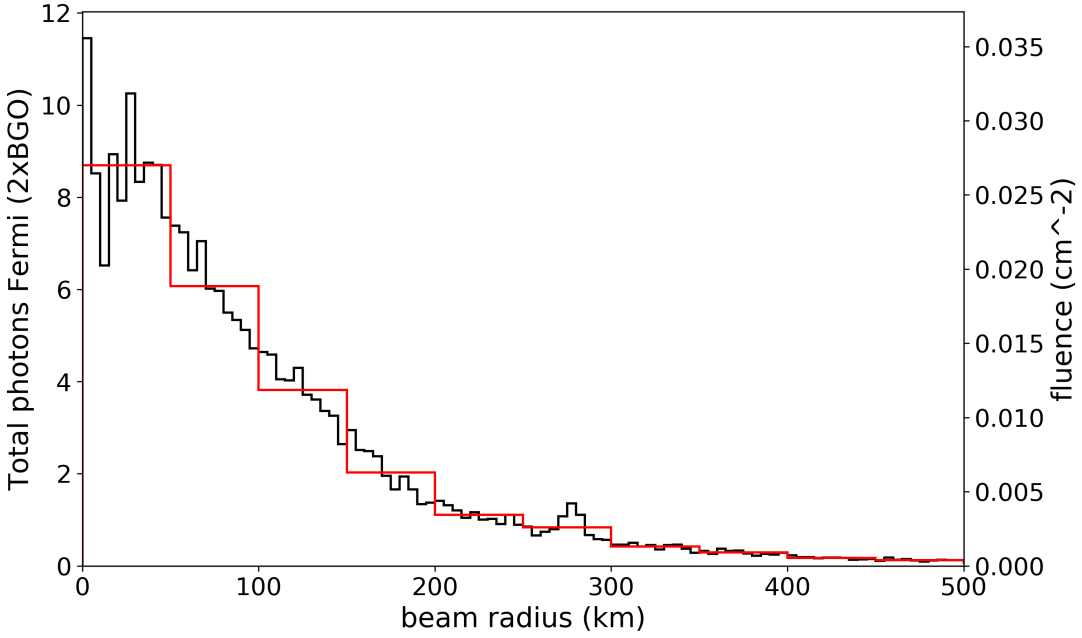

Figure 2.2: Black: Reverse beam gamma ray fluence of an 8km source altitude TGF simulation scaled to a 1.5×10^{18} main beam intensity binned in 5km wide annuli. Red: Same, binned in 50km wide annuli.

TGF luminosity observed from orbit will depend on how close the spacecraft is to the center of the beam. The horizontal distance between the NLDN best location and the Fermi/GBM is roughly 116km [Pu et al., 2020]. To obtain an estimate of the

minimum required intrinsic luminosity we will assume an optimally favorable tilt of the TGF such that the Fermi satellite falls within a 50km annulus of the reverse TGF beam center. See figure 2.1 for a qualitative description of our proposed scenario. Within 50km from the beam center the simulated fluence was relatively constant and begins to fall off outside of the 50km radius. Figure 2.2 shows the simulated reverse beam gamma ray fluence of an 8km source altitude TGF scaled to a 1.5×10^{18} gammas >1MeV main beam intensity binned in both 5km and 50km wide annuli. Pu et al. (2020) notes that only the counts from the two BGO detectors of the Fermi/GBM were used in the timing alignment procedure. For a TGF-like spectrum the effective area of the BGO detectors is 161 cm^2 [Tierney et al., 2013]. Multiplying the effective area by the fluence and limiting the calculated fluence to photons greater than 300keV, the low energy limit of the BGO detectors [Briggs et al., 2013], we derive the probable number of simulated photons incident on each detector.

2.4 Refined Altitude Estimate

The timing alignment method demonstrated by Pu et al. (2019) used the assumed simultaneity between the TGF electron avalanche and subsequent gamma ray observations with the 'slow pulse' observed in the LF and VLF sensors. Using the two dimensional (geographic) NLDN best location the arrival times of each signal were corrected for time of flight and the time difference between the centroids of each was determined. The altitude which minimized this time difference gave the best estimate

for the TGF source altitude. Any uncertainty in the analysis of Pu et al. (2020) came from the NLDN error ellipse of the associated lightning event. Locations along the perimeter of the ellipse are used to determine a minimized delta time between the signals by adjusting the altitude up or down from the source altitude derived from the NLDN best location. This alignment procedure was done for the reverse beam observation published in Pu et al. (2020) and is the justification for the 5.7-6.4 km TGF source altitude estimate.

We add two additional components to this timing analysis. First, there is an uncertainty in the gamma-ray arrival times at the Fermi/GBM that was not taken into account in the original analysis. The 8 counts incident on the BGO detectors should be considered a random sample from an unknown parent distribution. The mean of which will vary with respect to the sample mean. Assuming a Gaussian parent distribution, the standard deviation of the mean (centroid) of the BGO counts is the standard deviation σ of the sample population divided by the square root of the number of counts N in the sample population or $\frac{\sigma}{\sqrt{N}}$. The error in the centroid of gamma-ray arrival times is ± 8.2 μs. Converting that timing error into a distance uncertainty between the Fermi/GBM and the TGF source gives ± 2.5 km. When added in quadrature to the NLDN uncertainty the estimated source altitude range of the TGF broadens from 5.7-6.4 km to 3.4-8.6 km.

The second addition is to redo the timing alignment using an alternate NLDN location. The original analysis uses the NLDN location for the return stroke of the -CG

event. As described in Pu et al. (2020) the 'slow pulse' occurs 3 ms prior to the return stroke with the initial breakdown pulses (IBPs) occurring 3 ms prior to that. Using a typical CG leader progression speed of 10^6 m/s and the time from IBPs to return stroke of roughly 6 ms, the negative leader tip would have been at an altitude of 3 km when the Fermi reported TGF occured. Considering the leader tip would further travel to less than 1 km from the ground when the return stroke occurred Pu et al. (2020) argues that the most likely scenario is that the TGF was produced nearer to the initiation point, possibly associated with the positive polarity end of a bidirectional CG leader. NLDN recorded an event 6 ms prior to the return stroke with a significantly smaller peak current and horizontal distance of 1.7 km from the return stroke which we believe to be the initial breakdown pulses (IBPs) of this event. This NLDN location (26.6378,-77.2002) is our best estimate for the location of the TGF though the positive polarity leader may have traveled some distance horizontally from this location within the 3 ms time difference between the IBPs and TGF. Redoing the timing alignment analysis with this new location results in an estimated source altitude of 7.5 km with a range of $\pm$2.6 km when taking into account both the NLDN and Fermi/GBM uncertainty.

2.5 Meteorology

To determine if the source altitude estimate derived in section 2.4 is consistent with where we might expect the charge centers of the storm cell we use a High-Resolution Rapid Refresh (HRRR) model [Dowell et al., 2022] of a nearby storm cell. The TGF

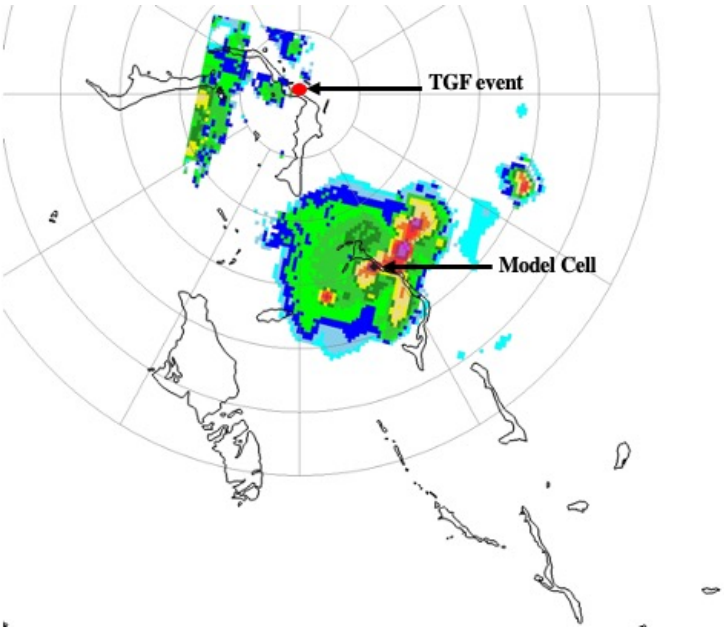

Figure 2.3: Composite reflectivity of the HRRR model cell at 0200UTC. Range rings in 50 km increments are centered at the July 25 event. The model cell is close to land, similar to the TGF location, but an adjacent island.

event was observed by Fermi at 02:23:12.82895 UT on 25 July 2019. The modeled storm cell was located 150 km from and just prior (0200UTC) to the July 25 event. In figure 2.3 you can see that the model cell is close to land, similar to the TGF location, but near an adjacent island. Figure 2.4 shows a scatter plot of all NLDN lightning event peak currents that occured within 20 minutes and 10km of the -CG TGF associated event (red). The NLDN events are identified as either CG (black) or IC (blue). There is a clear dominance of -CG events during this time period suggesting a typical tri-pole charge structure of the storm. A relatively weak lower positive, main lower (middle) negative and a main upper positive.

Hydrometer mixing ratios were used to assess non-inductive charging of the model cell as a function of cloud water content, ice crystal content, graupel content and

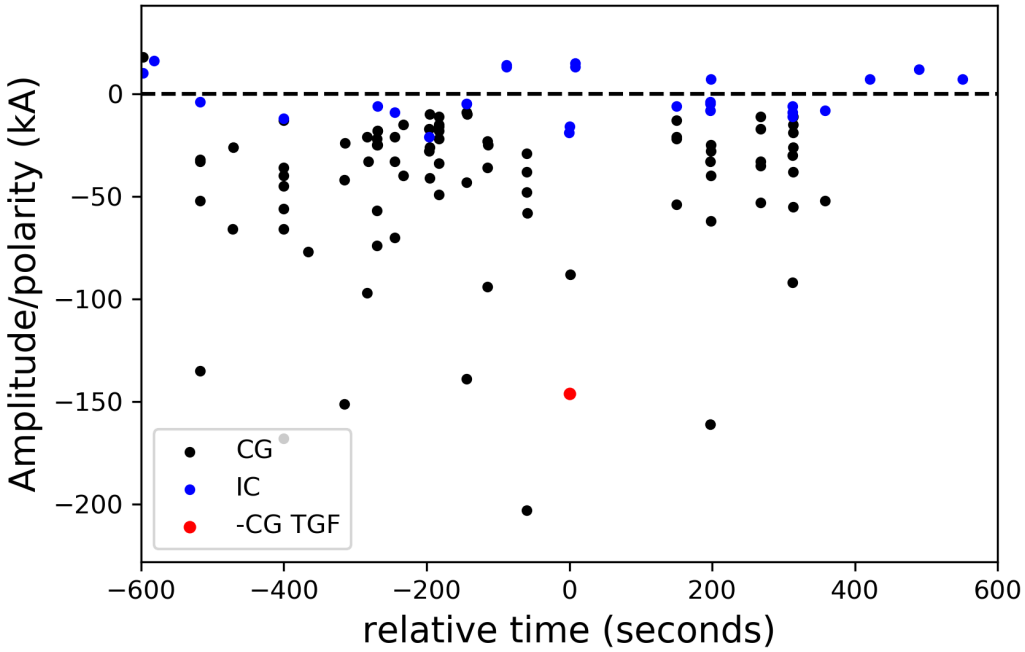

Figure 2.4: Peak current of all NLDN lightning events (CG in black. IC in blue) within 20 minutes and 10 km of the -CG flash associated with the TGF (red).

temperature [Takahashi, 1978; Jayaratne et al., 1983]. When ice crystals collide with graupel in the presence of supercooled water droplets, charge is transferred between these ice particles so that they are left with either a surplus or deficit of electrons following the collision. The vertical profile of the 0200UTC model cell is plotted in Figure 2.5. The shaded region in Figure 2.5 represents the altitudes where liquid water content, (CLMR, purple), graupel (GRLE, red), and ice crystals (CIMR, green) are substantially present and non-inductive charging would be expected. Below the -15C reversal temperature and where graupel (GRLE, red) has its peak around 6km is a likely center for positive charging (positively charged graupel). Above the -15C temperature altitude where the snow mixture (SWMR orange) peaks at 8km is the likely center

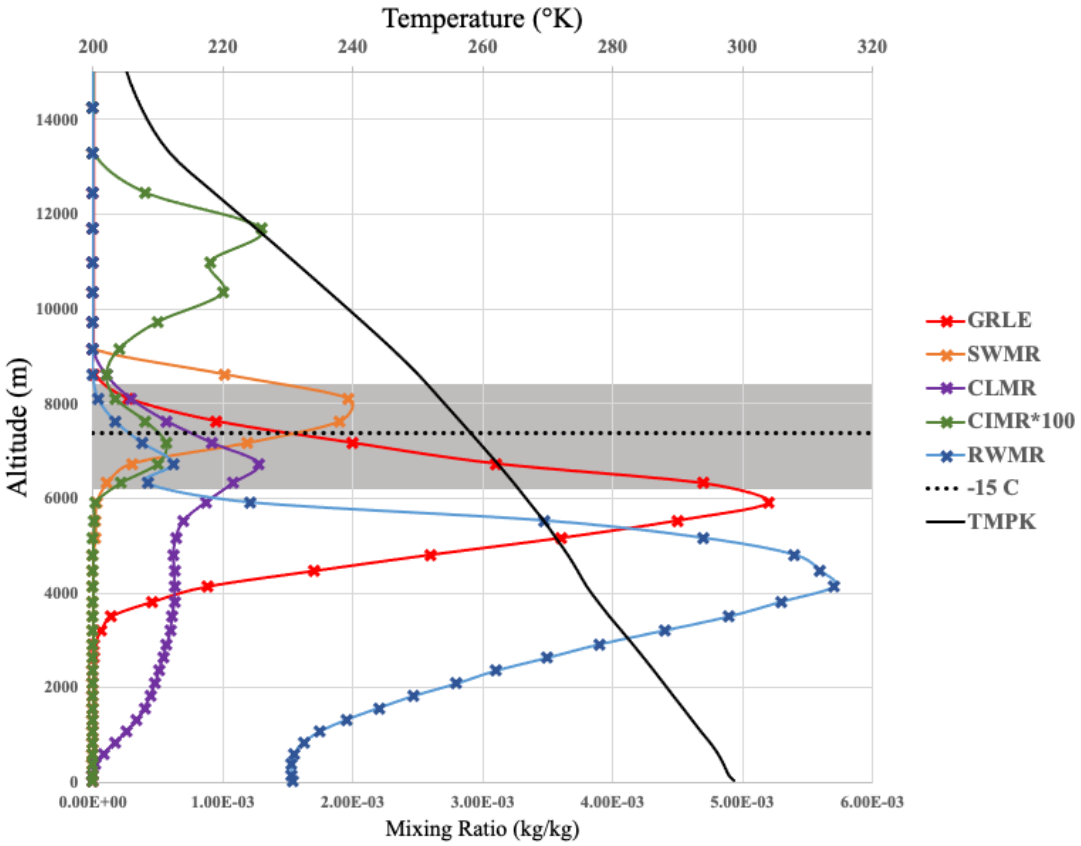

Figure 2.5: Graupel Mixing Ratio in red, Snow Mixing Ratio in orange, Cloud Water Mixing Ratio in purple, Cloud Ice Mixing Ratio in green but multiplied by 100 to be visible on plot, Rain Water Mixing Ratio in blue, and Air Temperature in black. Shaded region denotes altitude range with highest percentages of cloud water content (Purple), ice crystals (green) and graupel (red). Positive charging at 6300 m. -15°C 'reversal temperature' (dotted black line) at 7000 m. Negative charging at 8000 m.

for negative charging. Considering the model storm cell was part of the same weather system, close in time and location, to the the storm cell that produced the TGF it is liekly that the TGF producing cell was developing an electric field roughly between 6 km and 8 km pointed upward, consistent with a bi-directional CG leader moving negative charge downward. Though the source altitude uncertainty from section 2.4 extends up to 10 km the charging analysis suggests that TGF source altitude estimates above 8 km become less likely as electron avalanches in that altitude range would likely be directed

upward away from the negative charge center and toward an upper positive.

2.6 Simulation Results

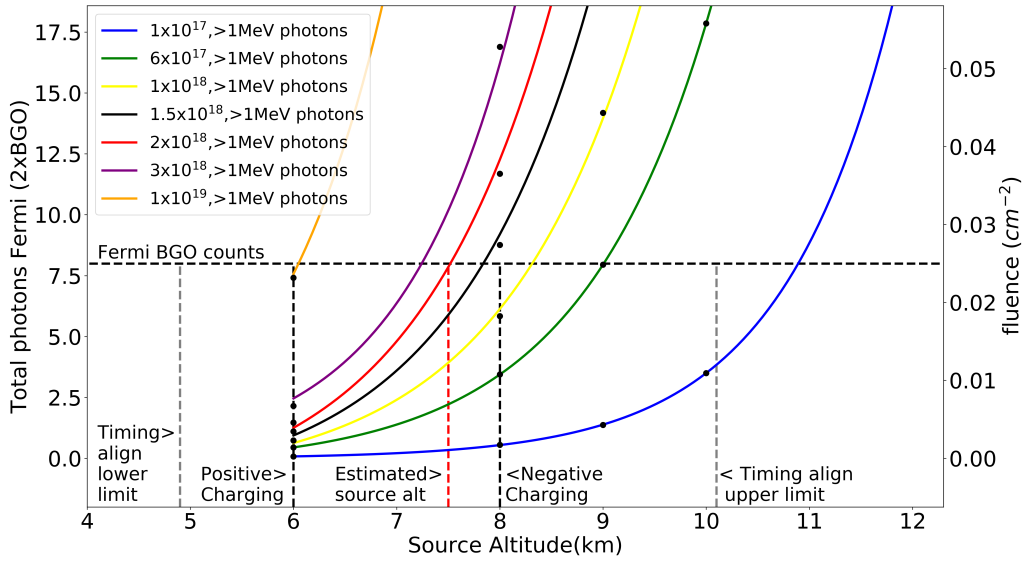

Figure 2.6: Data points represent the averaged simulated reverse beam fluence within an annulus of 50 km from beam center captured at an orbital altitude of 530 km. A curve is fit to data points of the same intrinsic brightness. Horizontal dashed line indicates the number of counts incident on the two Fermi BGO detectors of the July 25 event. The vertical dashed red line indicates the source altitude estimate of 7.5 km as derived in section 4. The two vertical black dashed lines indicate the likely positive and negative charge center altitudes. The two vertical grey dashed lines indicate the uncertainty in the TGF altitude estimate from timing alignment of the radio and gamma ray centroids.

The results of the REAM Monte Carlo simulations are presented in Figure 2.6. Each data point represents the averaged simulated reverse beam fluence as a function of source altitude and intrinsic brightness of the main beam, within an annulus of 50km from beam center and captured at an orbital altitude of 530 km. A curve is fit to data points of the same source luminosity using the expected exponential model of radiation

transport through matter. The vertical dashed red line indicates the source altitude estimate of 7.5 km as derived in section 2.5. A TGF at 7.5 km is consistent with the HRRR model cell analysis locating the TGF to just below the altitude estimate of negative charging in the model storm cell. This supports the scenario of a positive polarity leader propagating upward toward a negative charge center resulting in A TGF [Dwyer et al., 2004; Hare et al., 2016; Smith et al., 2018]. At this estimated source altitude the lower limit on the intrinsic brightness of the TGF, to be consistent with the minimum fluence required for a Fermi/GBM detection, is roughly 2×10^{18}.

2.7 Discussion

Is this brightness estimate reasonable? Although the reverse beam has 1% of the photons of the forward beam, it is more concentrated in the central 50 km annulus and higher in average energy and therefore more penetrating [Bowers et al., 2018; Ortberg et al., 2020].There are several examples in the literature of TGFs with luminosities at similar orders of magnitude [Mailyan et al,. 2016, Smith et al., 2020] to our estimate of 2×10^{18}. In particular, we reference a TGF over the Mediterranean basin estimated to be as bright as 3×10^{18} [Gjesteland et al., 2015]. And though our estimate assumes an optimal beaming angle, the actual angular offset between Fermi and the vertical of the source position is only 12.5°. With an angular band corresponding to the inner 50 km annulus of approximately 5.5° the TGF would only need to be offset from vertical by 7° to be optimally beamed. With an average angular offset of roughly 30°

between Fermi and the Fermi catalogue of TGF source locations it makes sense that the first known orbital observation of a reverse beam TGF is one where optimal beaming is likely.

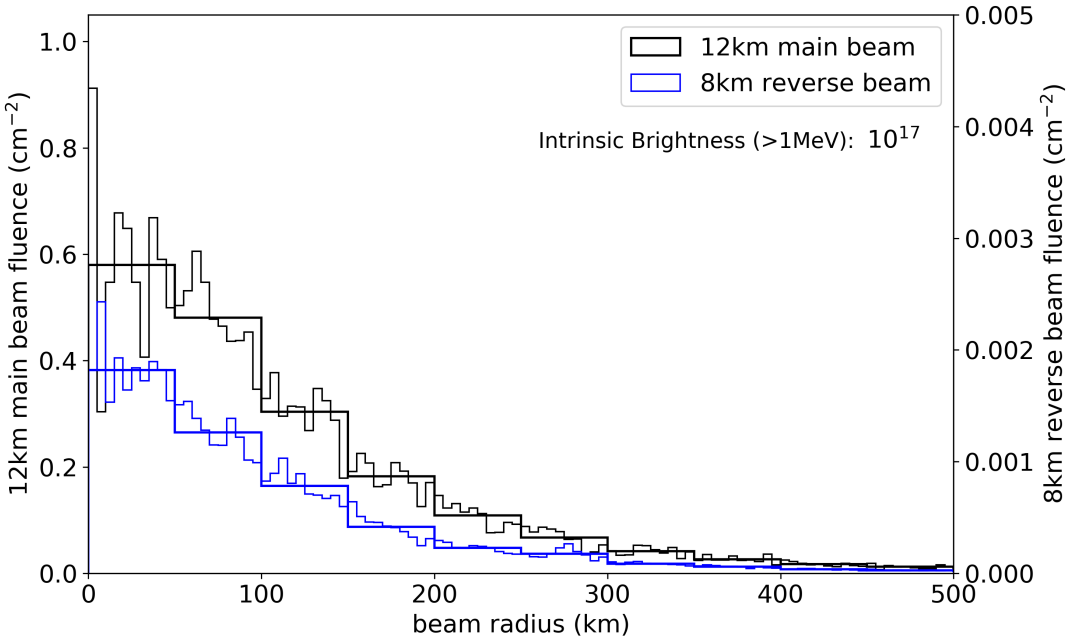

Figure 2.7: Black: Gamma ray fluence captured at 530 km from a 12 km upward TGF scaled to an intrinsic brightness of 10^{17} photons >1 MeV binned in both 5 km annuli and 50 km annuli. Blue: Gamma ray flux captured at 530 km from an 8 km reverse beam of a downward TGF scaled to an intrinsic brightness of 10^{17} photons >1 MeV binned in both 5 km annuli and 50 km annuli.

We thought at first it would be impossible for a TGF that was deeper in the atmosphere than any previous orbital observation, and considered to be the reverse beam component of the TGF, to be visible. As a check on the results of our simulation we define a 'typical' upward TGF Fermi/GBM observation as having a source altitude of 12 km, intensity on the order of 10^{17} photons >1 MeV, a median radial distance from the Fermi/GBM of 311 km [GBM Terrestrial Gamma-ray Flashes (TGF) Catalog], and having an average count rate of roughly 50 counts including both BGO detectors and

the sum of the NaI detectors for TGF duration's less than 200μs [Briggs, 2013]. REAM Monte Carlo simulations, using our atmospheric model, of this typical TGF show a simulated fluence of 0.05 cm^{-2} at the typical 311 km annulus consistent with previous analysis of typical orbital TGF fluence rates on the order of 0.1 cm^{-2} [Dwyer et al. 2017; Ostgaard et al. 2012].

The ratio between the 50 km beam center of the 12 km upward TGF and an 8km reverse beam of a downward TGF with the same intrinsic luminosity is roughly 350 (See figure 2.7). In other words, for the reverse beam TGF to attain an equivalent fluence within the center of the beam at orbital altitudes to a typical 12km upward TGF at beam center the 8km downward TGF would need to be 350 times brighter or 3×10^{19}, well beyond any previously published estimates of observed TGF luminosity. However the 12 km upward fluence at its 311 km annulus is only 35 times brighter than the 8 km reverse beam fluence at beam center, meaning the 8km downward TGF would need to be 35 times brighter for the reverse beam with optimal beaming angle to be observed by Fermi with a count rate typical of Fermi observations. But the total counts of the July 25 event (8 BGO counts + 10 Nai counts) is roughly $\frac{2}{5}$ our definition of a typical Fermi TGF count rate. Thus a downward TGF at 8 km would only need to be $(35\times\frac{2}{5})$=14 times brighter than our defined typical upward TGF giving a brightness estimate of 1.4×10^{18} at 8 km, consistent with our estimate of 2×10^{18} for a 7.5 km downward TGF.

2.8 Summary

The proposed scenario [Pu et al., 2020] of a bi-directional CG leader initiating at 6-7 km resulting in a downward directed TGF from the upward propagating positive leader, whose reverse beam component was observed by Fermi/GBM, seems likely. The estimated negative charge center altitude just under 8 km is consistent with our best estimate of the source altitude of the TGF at 7.5 km. We have also shown, using Monte Carlo simulations, that the reverse beam of this TGF is detectable from orbit under ideal beaming conditions with an estimate of the lower limit of intrinsic brightness being bright but not without precedent.

Section 3

Säntis Mountain TGFs

Mountaintop gamma ray observations of three TGFs at the Santis Tower, Switzerland with coincident radio waveforms

Jeffrey M. Chaffin, David M. Smith, Jeff Lapierre, Steve Cummer, Marcos Rubinstein, Farhad Rachidi, Antonio Sunjerga, Amirhossein Mostajabi

3.1 Abstract

We report on the mountain top observation of three TGF events that occurred during the summer storm season of 2021. To our knowledge these are the first TGFs observed in a mountain top environment and the first published European TGFs observed from the ground. A gamma-ray sensitive detector was located at the base of the Säntis Tower in Switzerland and observed three unique TGF events with coincident radio sferic data characteristic of TGFs seen from space. We will show an example of

a 'slow pulse' radio signature [Cummer et al.,2011; Lu et al.,2011; Pu et al.,2019, Pu et al. 2020], a -EIP [Lyu et al.,2016,2021a; Cummer et al.,2017; Wada et al. 2020], and a double peak TGF where each TGF peak is possibly preceded by a short burst of stepped leader emission.

3.2 Introduction

Terrestrial gamma ray flashes (TGFs) are submillisecond bursts of radiation (up to 10's of MeV) generated in thunderstorms and closely associated with lightning [Fishman et al., 1994, Cummer et al. 2005; Smith et al. 2005; Stanley et al. 2006; Briggs et al. 2010]. The source of the gamma ray production ,via the bremsstrahlung mechanism, is understood to be an exponentially growing population of relativistic electrons or relativistic runaway electron avalanches (RREA) within the electric fields associated with the lightning leader process and possibly to an unknown extent the local ambient field [Wilson 1925; Gurevich et al. 1992; Lehtinen et al. 1996; Dwyer 2003; Dwyer et al. 2012]. However, the mechanism of the Terrestrial Gamma Ray Flash and its connection to lightning leader propagation is not fully understood. This has led to a recent focus on multi-wavelength observations which can shed light on the temporal relationship between TGFs and radio signatures of different lightning processes.

The last decade has seen some compelling multi-wavelength observations in lightning leader (+IC) radio emission that have linked a subset of TGF satellite observations with

two specific types of radio waveforms during lightning leader propagation. 'Slow Pulse' events [Cummer et al.,2011; Lu et al.,2011; Pu et al.,2019; Pu et al. 2020], observed in the midst of initial breakdown pulses (IBPs) of relatively small peak current lightning events, are characterized by a distinct slow temporal signature matching the associated TGF duration and near simultaneous (within a few microseconds) with the mean of gamma ray arrival times. Dwyer and Cummer (2013) showed how this 'slow pulse' is predicted by the feedback TGF model and can be interpreted as an observable current moment of the TGF electron avalanche process itself.

The second kind of characteristic pulse, energetic in-cloud pulses (+EIPs) [Cummer et al.,2017; Lyu et al.,2016, 2021a], are high peak current sferics associated with negative leader +IC lightning. TGFs have been found to be time aligned (within about 10μs) with +EIP sferics tens to hundreds of microseconds long [Cummer et al., 2011; Lu et al., 2011].

These distinct classes of sferics give a unique perspective into the behavior of the TGF mechanism not possible with gamma-ray observations alone. Though the observation of -EIPs and negative polarity 'slow pulses' have been inferred to correspond with downward TGFs, thus far there have only been two published observations that directly make this connection, Pu et al. (2020) and Wada et al. (2020) which reported on a negative 'slow pulse' and -EIP respectively. In addition to these two associations we report on the mountain top observation of three TGF events, to our knowledge the first TGFs ob-

served in a mountain top environment. We will present multi-wavelength measurements making direct associations between two of the TGFs observed and low frequency radio sferic data of both a 'Slow Pulse' event and a -EIP. A third TGF observation appears to be a double pulse event coincident with a very unusual high peak current radio sferic, and was close enough to the tower to observe the neutron afterglow [Bowers et al., 2017; Enoto et al., 2017; Wada et al., 2019a, 2019b].

3.3 Instrumentation

A gamma-ray sensitive detector consisting of a 5 × 5" plastic scintillator mounted to a conventional photomultiplier (PMT) tube was located at the base of the Säntis Tower on Mt. Säntis, Switzerland at an elevation of 2.5km. The analog output of the PMT was routed to a Bridgeport Instruments eMorpho MCA. The MCA uses an 80 MHz ADC and provides a time-tagged photon event list mode with the integrated pulse area (with 16-bit resolution) and arrival time (with 32-bit/12.5 ns resolution). Earth Networks Total Lightning Network (ENTLN) provided geolocation of individual lightning flashes using an array of ground-based sensors located through out the European continent using low frequecy (LF) radio sferic data.

3.4 Measurement and Analysis

On 9th of June 2021 two TGFs were observed during a series of thunder storm cells passing over Mt. Säntis. Event 1 was a roughly 150 μs duration flash of gamma

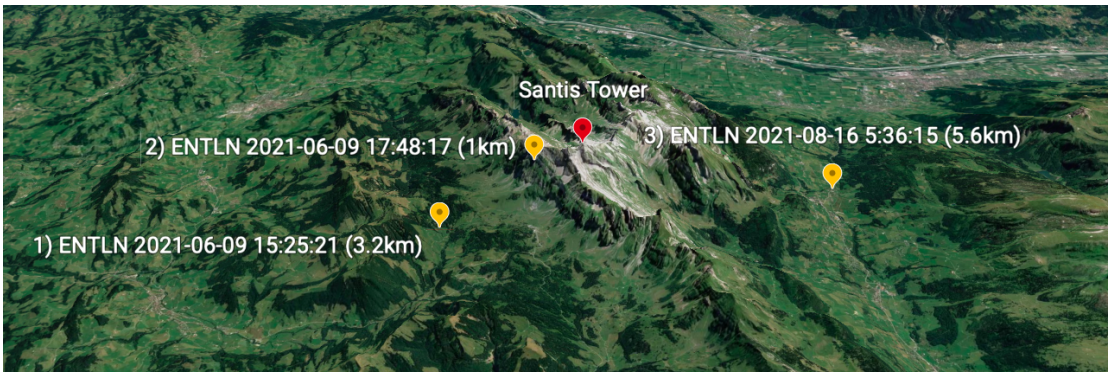

Figure 3.1: Earth Networks Total Lightning Network (ENTLN) geo-locations (yellow markers) for each event and distance from the Säntis Tower (red marker)

photons coincident with a -IC (-10kA) lightning leader at 15:25:21.165148 UTC with an ENTLN location of 3.2 km from the Säntis Tower. Event 2 was a double pulse gamma ray flash lasting 400 μs in total. This second event was coincident with an unusually strong (100kA) and complex +IC sferic at 17:48:17.847036 UTC located 1km from the Säntis Tower. Event 3 occurred on the 16th of August 2021 coincident with a -135 kA lightning sferic at 5:38:15.3093 UTC and 5.6km from the Säntis Tower. Unfortunately at the time of these observations the instrument computer clock was malfunctioning and absolute timing can only be certain to 1-2 ms. This is sufficient to associate each event to a lighting flash but insufficient to say anything quantitative regarding the timing relationship between the TGF observation and leader progression with time alignment of the data alone.

3.4.1 Event 1

Event 1 is associated with a ENTLN radio sferic on 9th of June 2021 at 15:25:21.165148 UTC and 3.2 km from the Tower. The gamma ray observation was

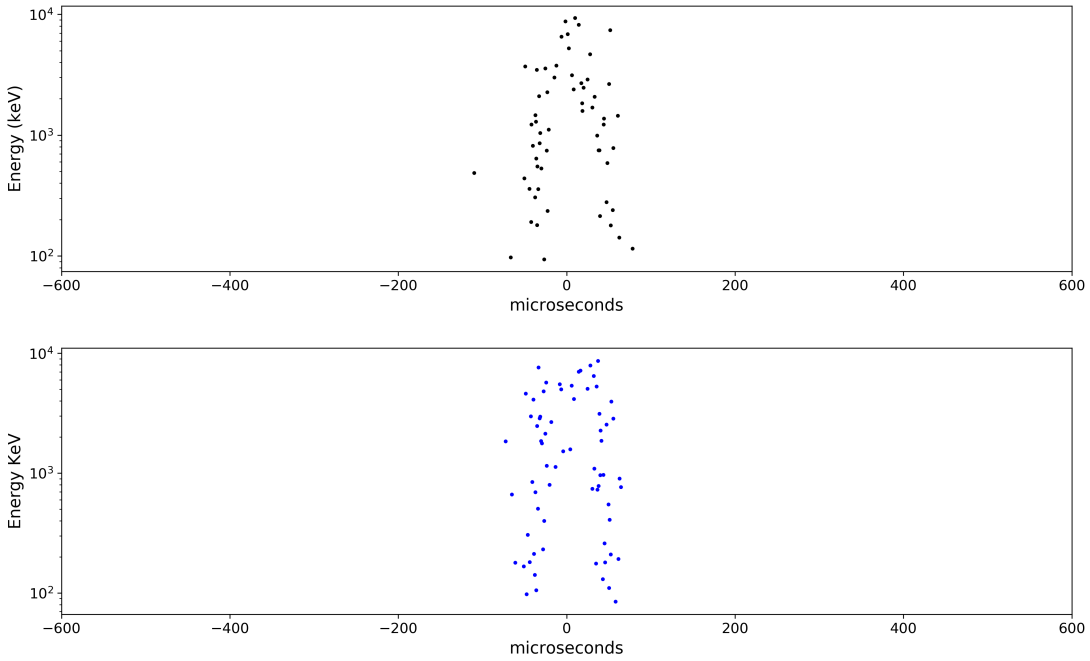

Figure 3.2: **Top**: TGF gamma ray energies versus time. Each black data point represent a 'single' photon count. The limited number and lack of low energy counts in the middle of the signal is a result of both deadtime and pileup in the detector electronics. The high energy counts in the middle of the scatter plot are likely a sum of several lower energy photons. **Bottom**: Simulated detector/electronics response to a TGF spectrum derived from a Monte Carlo simulation with temporal distribution and number of photon interactions in the detector adjusted to match the deadtime and pileup behavior of the TGF data plotted above.

roughly 150 μs in duration and produced 60 counts in the detector with an energy range of 100 keV to 9 MeV. Unfortunately there was significant pileup in the detector electronics during the brightest portion of the TGF resulting in a loss of counts and systematically giving the few recorded counts during the brightest portion artificially large energies. The sferic shows a negative polarity 'slow pulse' signal as described in Pu et al. (2019) but of opposite polarity indicating the movement of negative charge downward.

The pulse comes in the midst of short (<10 μs) IBPs and is similar in duration to the gamma-ray signal. If this radio sferic 'slow pulse' is a signature of the current moment of the RREA mechanism then the gamma ray duration should match the slow pulse duration. To determine this we follow the example of Pu et al. (2019) by attempting to fit the arrival time distribution of the gamma rays to a Gaussian under the assumption that the RREA current moment follows a normal distribution. The Earth networks sensors have a frequency response that is proportional to the radiative far-field electric field which is proportional to the derivative of the source current dI/dt. With the assumption that the current pulse produced by the RREA mechanism is Gaussian than the first derivative of the gamma ray arrival time distribution should be a good match to the 'slow pulse' in the Earth networks sensor data.

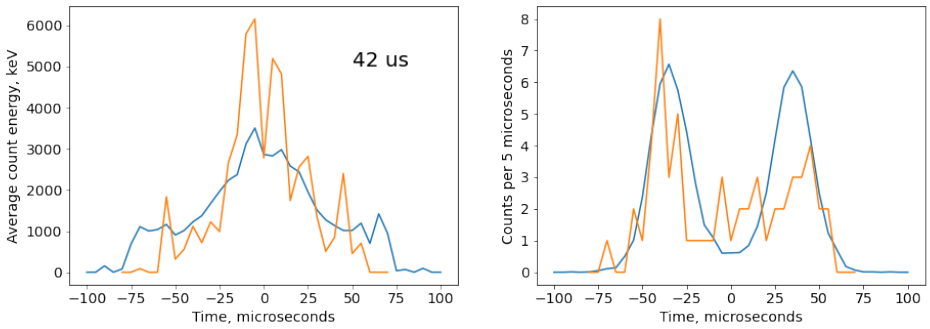

Figure 3.3: Left: average derived photon energy in each 5μs bin; Simulations in Blue and TGF data in orange. Right: number of counts in each 5μs bin; Simulations in blue and TGF data in orange

Unfortunately as mentioned previously the gamma ray data is significantly piled up during the brightest portion of the TGF. This makes determining an arrival time distribution challenging. We rely on a combination of GEANT4 [Agostinelli et al., 2003; Allison et al., 2006, 2016] Monte Carlo simulations of TGFs and python code

written to simulate the behavior of the PMT output trace and how the Bridgeport electronics processes the trace into individual photon counts. A TGF spectrum using the Relativistic Electron Avalanche Model (REAM) discussed in Dwyer (2003, 2007) and Dwyer and Smith (2005) was processed through a model of the atmosphere, U.S. Standard Atmosphere (1976), and finally through a model of a plastic scintillator to obtain a simulated energy spectrum in the detector.

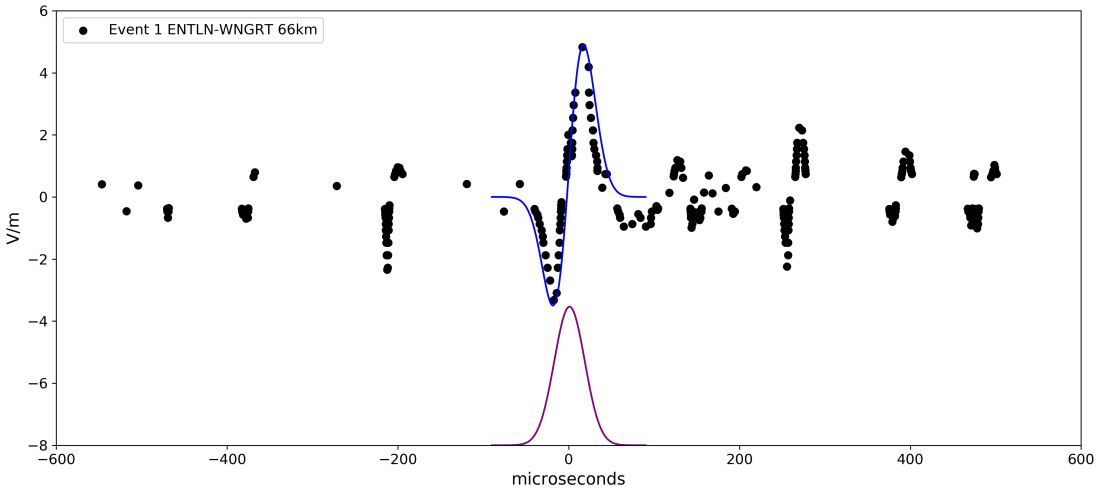

Figure 3.4: Event 1 radio sferic (black) of a -IC flash of -10 kA peak current. The first derivative (blue) of a 42μs FWHM Gaussian (Purple) is fit to the 'slow pulse' portion of the sferic. The LF sensor was 66km from the Santis Tower.

The spectrum was then spread out to a Gaussian arrival time distribution and used as input for the previously mentioned electronics simulation code. Two parameters, the width of the time distribution and the number of photon interactions in the detector, were adjusted until the simulation output matched the pile-up/dead time behavior, duration and number of counts in the TGF data. Figure 3.2 shows the TGF gamma ray energies versus time scatter plot in black (top plot) and the simulated TGF with

the electronics signal processing behavior accounted for (bottom plot) in blue. Figure 3.3 shows two plots that use a FWHM of 42 μs for the simulated TGF Gaussian and roughly 2000 photon interactions in the detector. In the simulations (blue) 100 different TGFs with random energy and time samples of this Gaussian parent distribution were used to average the curves together. The real TGF data are in orange. The plot on the left is the average derived photon energy in each 5 μs bin, showing the effect of pileup. The plot on the right is the number of counts in each 5μs bin, showing the duration and the effect of dead time. To the eye the 42 μs FWHM is a likely best fit with approximate errors of +/- 5 μs FWHM. In Figure 3.4 the first derivative of a 42 μs FWHM Gaussian is overplotted on the radio sferic 'slow pulse' data and aligned in time with the simulated Gaussian count rate distribution. The first derivative of the Gaussian is in good agreement with the 'slow pulse' confirming our assumption of a Gaussian source current derived from the gamma ray temporal distribution. Though the timing precision of the TGF observation isn't sufficient to time align the two data sets, the agreement between the sferic slow pulse and the first derivative of the Gaussian arrival time distribution along with the work done by Pu et al. (2019, 2020) is compelling evidence that this 'slow pulse' and gamma ray observation are the result of the same physical mechanism making this the first ground based TGF observation linked to a 'slow pulse' sferic.

3.4.2 Event 3

Event 3 took place on August 16, 2021. It was associated with an ENTLN lightning sferic at 5:38:15.3093 UTC that was located 5.6 km from the Säntis Tower. At that distance from the source the gamma ray observation (Figure 3.5 bottom) doesn't appear to suffer from pileup or deadtime but is outside the detection radius of any neutron signal. The associated radio sferic (Figure 3.5 top) was a very high peak current (-135 kA) -IC event. With the exceptionally large peak current, big clear pulse in the low frequency radio data, and clear negative polarity we immediately suspected this to be a -EIP. To confirm this we sought to compare a known EIP to the waveform associated with our gamma ray signal.

When comparing LF waveforms it is crucial to make sure the comparisons are being made using sensors that were an equal distance to the source of the signal. The reason for this is related to the propagation times of both the ground wave and the sky wave. The closer the LF sensor is to the signal source the greater the time difference between the arrival of each at the sensor. For instance, you can see in the top plot of Figure 3.5 the radio sferic of Event 3 as recorded by a sensor 256 km from the source. You can clearly differentiate the ground Wave signal lasting roughly 100 μs followed closely by the ionospheric reflection or sky wave.

In contrast, Figure 3.6 is from a sensor 425 km from the same source signal. The ground wave and its reflection are too close together to differentiate making the signal appear quite different. From a collection of unpublished EIPs confirmed by both

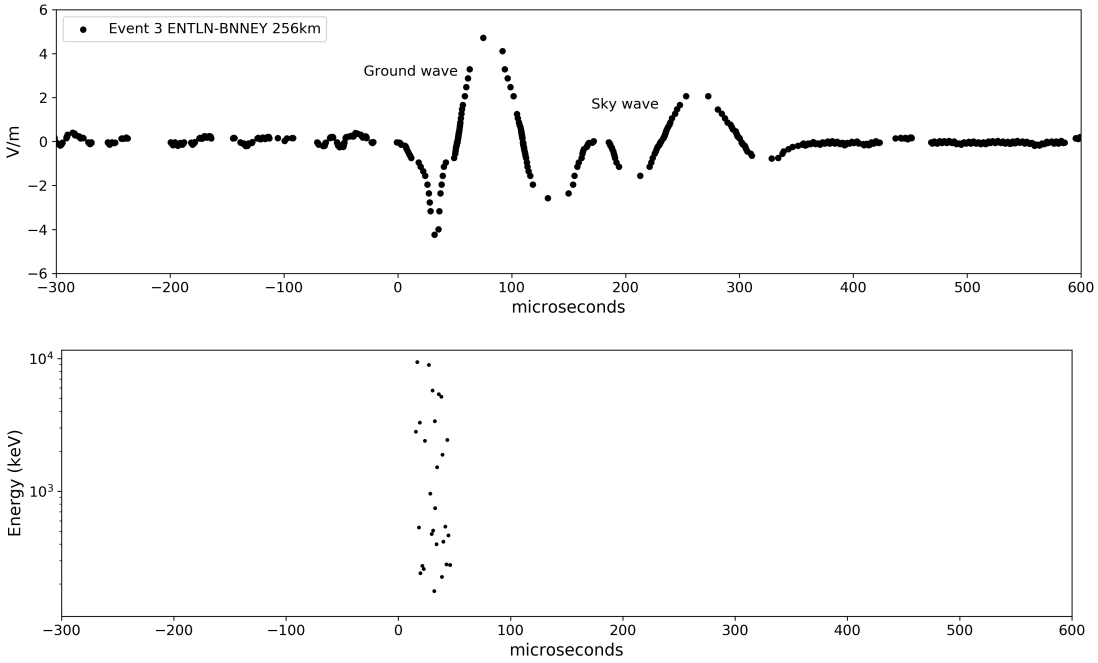

Figure 3.5: **Top**: Event 3 radio sferic of an -IC flash with 135 kA peak current. The flash was located 5.6 km from the Säntis Tower. The radio data is from an LF sensor 256 km from the flash. **Bottom**:TGF counts plotted by energy vs time. Note that the timing alignment between the radio sferic and gamma ray data is purely speculative. We have aligned the 50 μs of gamma ray counts with the initial 50 μs of the ground wave.

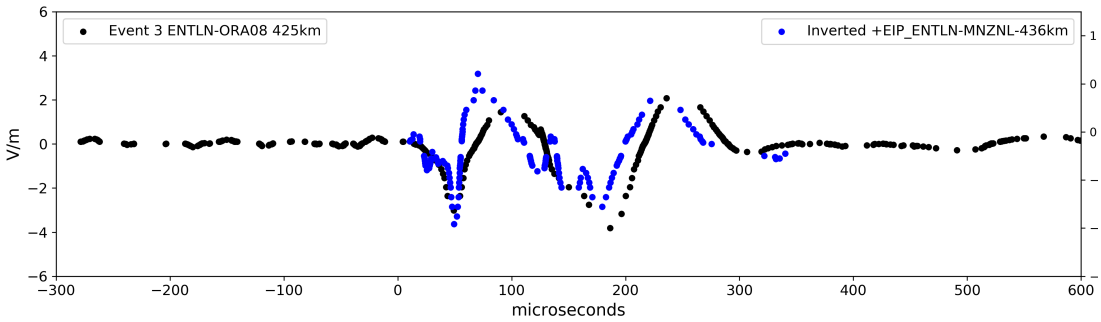

Figure 3.6: Event 3 radio sferic (black) using radio data from an LF sensor 425 km from the current source. Known +EIP (blue) from an ENTLN sensor 436 km from it's current source. The known +EIP data has been inverted and over plotted onto the Event 3 waveform for comparison.

Duke University sensors and Earth Networks we found a +EIP observation from a sensor 436 km from the signal source. We inverted the polarity of the known +EIP

data and over plotted it on the Event 3 sferic of a 425 km distant sensor as seen in figure 3.6. The signals are remarkably similar except for the polarity inversion of the known EIP which indicates the source currents are also similar. We believe that the Säntis signal is consistent with a -EIP produced during a descending negative leader or upward propagating positive leader.

3.4.3 Event 2

Event 2 is associated with a large amplitude (100 kA) +IC radio sferic on 9th of June 2021 at 17:48:17.847036 UTC. The ENTLN location puts the lightning flash 1 km from the Säntis Tower. The radio waveform (Figure 3.7 top plot) is atypical of an IC radio sferic. It has an unusually high frequency of large amplitude pulses. The pulse durations of 100-150 μs are much longer than normal IBPs and the spacing of the largest-amplitude features matches the spacing of the TGF pulses as shown by the speculative alignment with the gamma ray data in Figure 3.7. The ENTLN sensor was only 256 km from the lightning location. At that distance the ground wave signal will dominate the associated sky wave. This suggests that the equally large amplitude pulses in this sferic represent distinct current pulses in the lightning event.

This was an extraordinarily powerful sferic compared to other flashes in the local environment. Figure 3.8 depicts the 14 highest peak current events identified as +IC by the European Cooperation for Lightning Detection (EUCLID) in the prior year (2020) within 30km of the Säntis Tower out of a total database of 4598 +ICs in that distance range. The sferic data is from the same ENTLN sensor as our TGF-associated

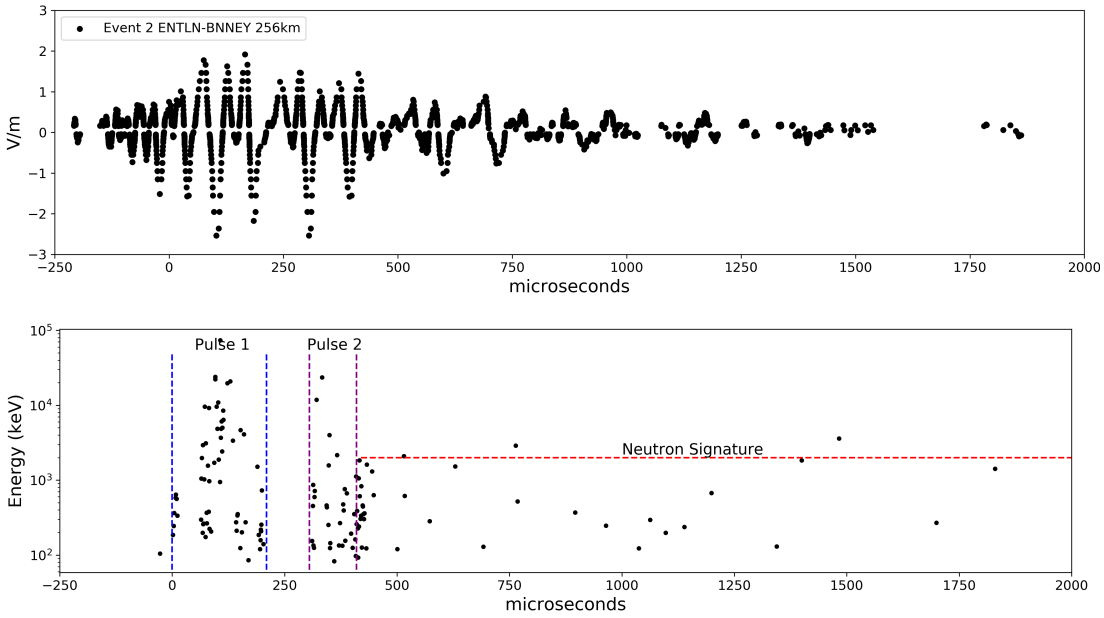

Figure 3.7: Top: Event 2 radio sferic of an +IC flash with 100 kA peak current. The flash was located 1km from the Säntis Tower. The radio data is from an ENTLN LF sensor 256 km from the flash. Bottom: TGF counts plotted by energy vs time. Possible double pulse event with a neutron after glow starting at 400 μs. Note that the timing alignment between the radio sferic and gamma ray data is purely speculative. We have aligned the 400 μs of gamma ray counts with the 400 μs duration of the large peak amplitude and wide pulse width radio data.

sferic shown in red at the bottom, and the distances between the current source and sensor vary between 245-291 km. Qualitatively it is quite obvious how distinct the TGF associated trace is to the sample of high peak current traces in proximity to Säntis Tower.

In order to quantify the uniqueness of this sferic we calculated the sum of the square of the E-field values, a measure of total radiated energy, that were recorded for each trace and plotted those values against each trace's peak current as shown in figure 3.9. The peak current is calculated by ENTLN from the single largest amplitude pulse (E-field measurement data point) in a trace. The TGF associated event has a $\sum E^2$

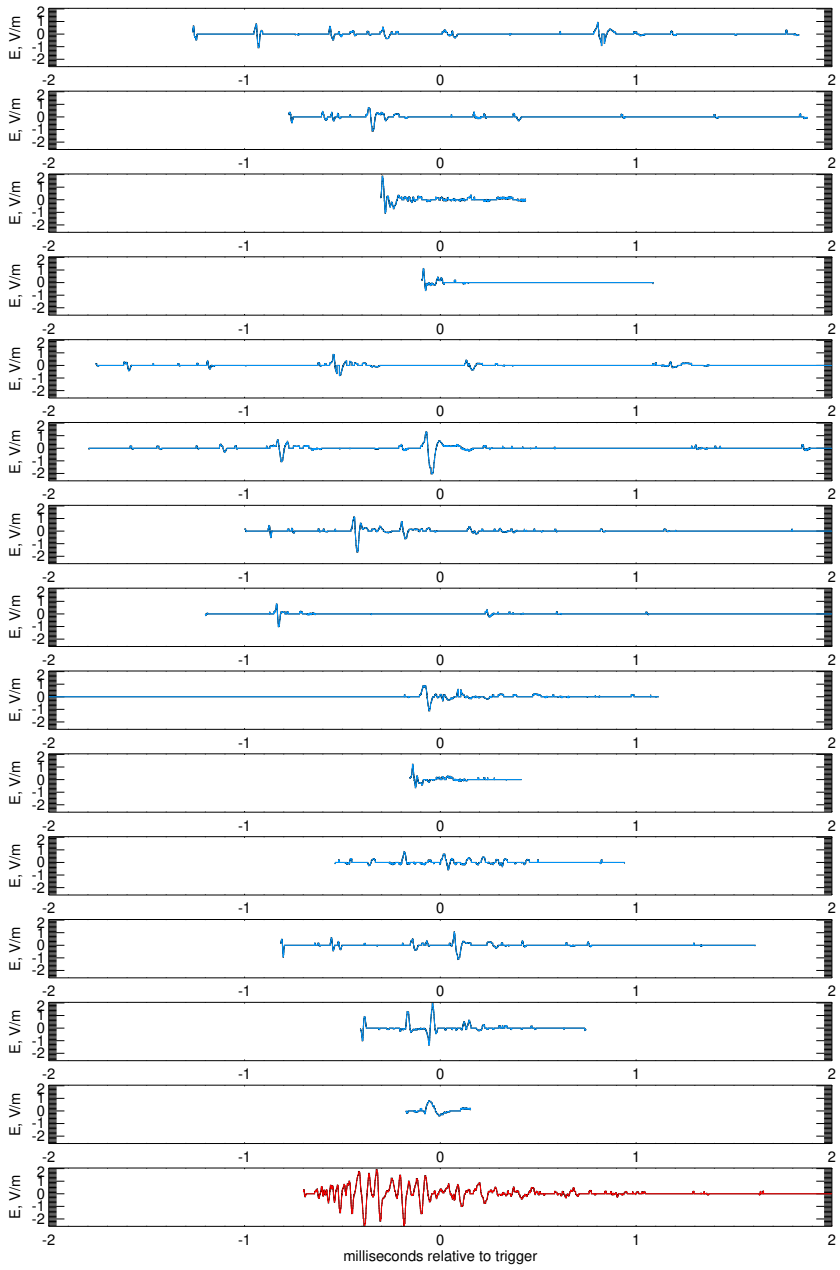

Figure 3.8: ENTLN radio data of the 14 largest peak current lightning events, within 30 km of the Säntis Tower from October 2019 - April 2021, and the Event 2 waveform in red. All traces are from the same ENTLN sensor at similar distances from the current source.

that is 5 times as large as its nearest competitor while the rest are clustered together. This does a nice job of capturing the unusualness of the event. Not just that it reaches a high peak current, and not just that it has many pulses, but that it has many pulses at an equally high peak current.

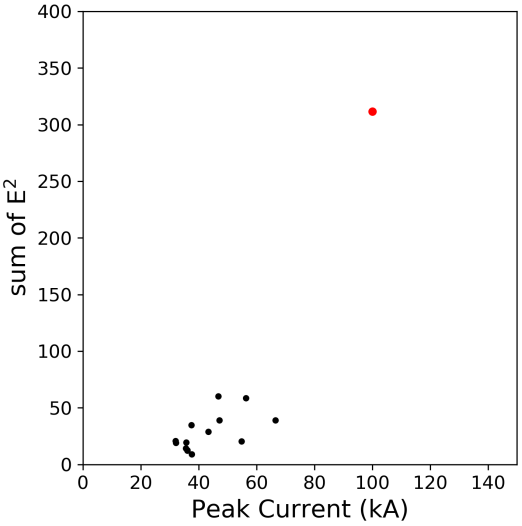

Figure 3.9: Sum of the square of the ENTLN electric field data for each trace in figure 8 plotted with respect to each events peak current. The 14 highest peak current events are plotted in black and roughly clustered in the same region of the plot, where as the Event 2 trace is plotted in red.

From the gamma ray data (see figure 3.7 bottom plot) the TGF appears to be a two peak event, but with significant pile-up and possible periods of detector paralysis. There is also a clear neutron tail of about 1.5 ms in duration. Downward TGFs during winter thunderstorms in Japan have been shown to produce a number of neutrons via photonuclear reactions in the atmosphere [Bowers et al., 2017; Enoto et al., 2017; Wada et al., 2019a, 2019b]. The thermalized neutrons with time scales on the order of milliseconds [Babich, 2006, 2007] interact in our plastic detector material and undergo neutron capture with hydrogen resulting in the hydrogen isotope deuterium in an excited

state. The excited deuterium immediately relaxes to its ground state emitting a 2.2 MeV gamma in our detector. The 2.2 MeV gamma deposits only a portion of its energy via Compton scattering before leaving the detector material resulting in a Compton shoulder at roughly 2 MeV.

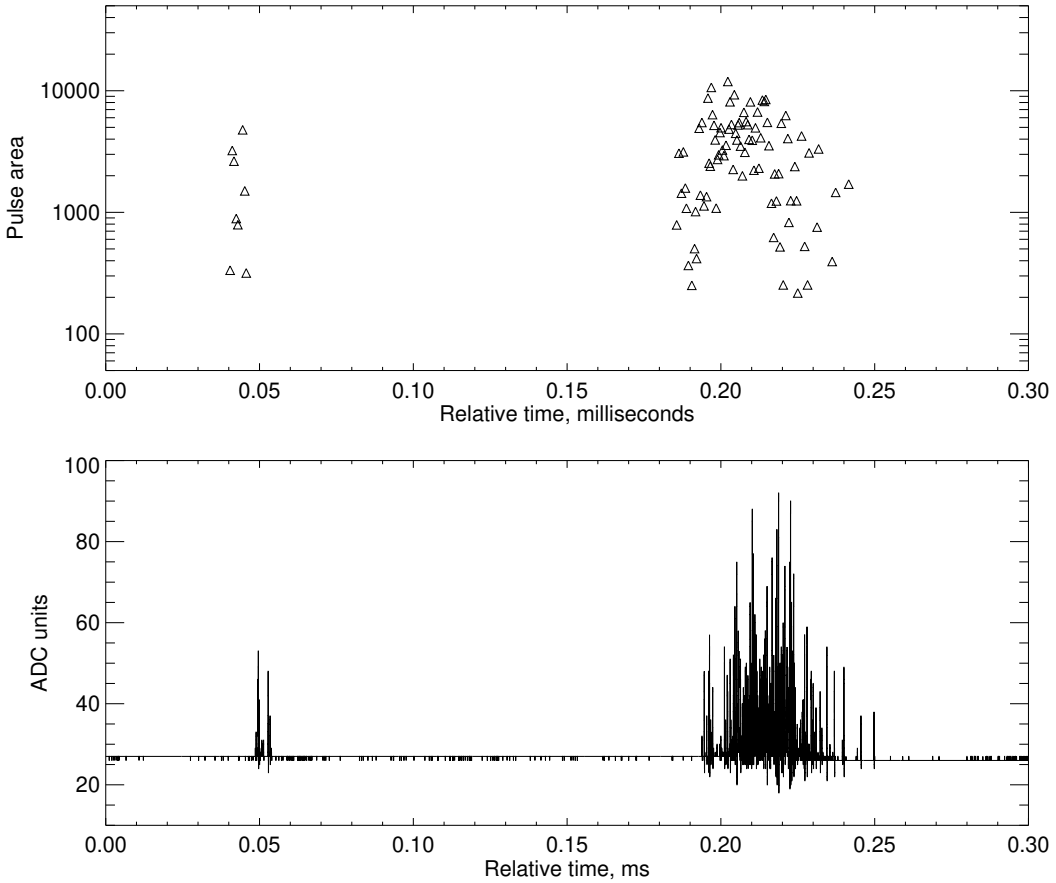

Figure 3.10: Unpublished data from the Terrestrial High energy Observations of Radiation (THOR) instrument deployed on Mt. Fuji, Japan in the summer of 2022. Top: Scatter plot of integrated pulse value (Energy) vs time of the photon event list data. Each data point ideally represents a single photon count. Bottom: ADC sampled trace data of the analog PMT output or pulses for the same time period as the upper scatter plot.

Figure 3.10 is unpublished data from the Terrestrial High energy Observations of Radiation (THOR) instrument deployed on Mt. Fuji, Japan during the summer of

2022. THOR is a more advanced instrument with the ability to save 300 μs of the PMT trace data for high count rate events along with the continuously running photon event list of the integrated PMT pulses. One of the benefits of having trace data is being able to conclusively assess periods of detector paralysis vs real time gaps between signals. You can see in the THOR photon list mode data (figure 8 top plot) a short burst of counts preceding the main TGF by rougly 150 μs. The trace data (figure 8 bottom plot) confirms that the time gap between the two signals is real and not a result of detector paralysis. Further, what can't be seen in the list mode photon data but is evident in the trace data is a possible second short burst of photons, just before t=0.20 ms, directly preceding the count rate increase of the TGF and the piled up behavior at the point of largest count rate. This observation will be published in a future paper and we believe it shows a connection between stepped leader X-rays and TGFs.

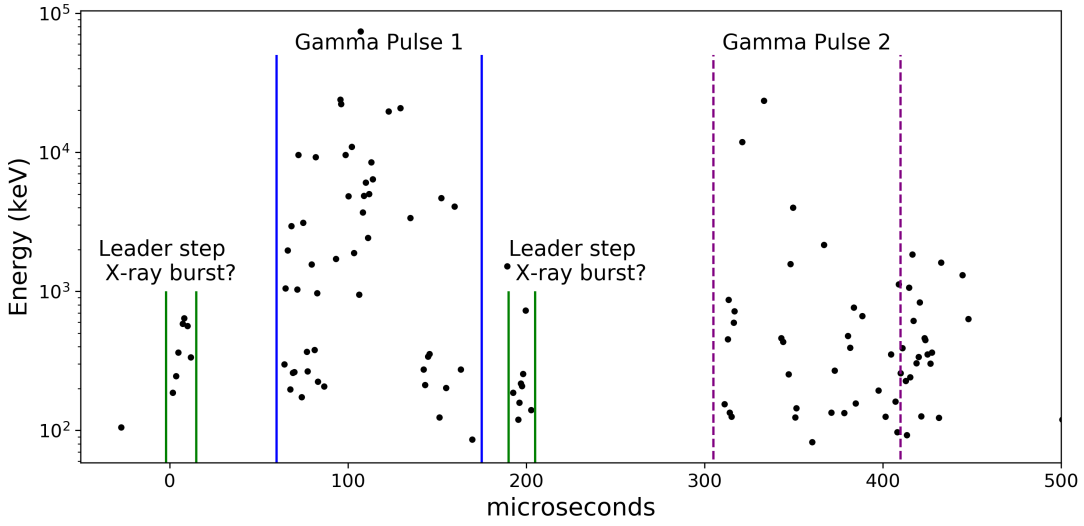

Figure 3.11: Event 2 double pulse TGF listmode gamma ray data. Speculative interpretation of four separate x- and gamma-ray emissions within the 400 μs duration of the event. Two possible stepped leader bursts each preceding one of the two TGFs.

We've included this unpublished THOR observation to give context to an interpretation of the Mt. Säntis photon event list data. Figure 3.11 shows the roughly 400 μs of the double pulse TGF. It is possible that there are actually four distinct signals. The first could be a stepped leader emission that precedes the initial TGF by about 60 μs. The TGF is about 150 μs in duration and the data exhibits detector paralysis and pulse pile up behavior, a period of no low energy counts (not real), as the count rate increased. As we begin to see low energy counts again we assume that the count rate is decreasing. This is followed by a 20 μs gap before a second short burst of photons (stepped leader emission?) that precedes the second TGF pulse by 120 μs. Without the trace data to confirm the instrument behavior this interpretation remains speculative but possibly very important.

A possible explanation for the unusualness of the Event 2 waveform may be directly connected to the multi-pulse TGF observation just described. Could this be a multi-pulse +EIP? We know Event 3 to be an example of a confirmed -EIP observed by the same radio sensor as Event 2 and from an equivalent distance from the source. We compare the Event 2 waveform to the Event 3 -EIP by inverting the Event 3 sferic and summing two versions of the inverted data but separated in time. In Figure 3.12 you'll see the green dashed lines that are separated by 210us. That appears to be the time separation between the most piledup-paralyzed moments in each TGF pulse. That comes earlier for the 2nd pulse, which is why it is shorter than the delay between the starts of the pulses. Top panel is Event 3 inverted. Middle panel has two "Event 3s" spaced by 210 μs and summed. The bottom panel is Event 2. It is of course speculative

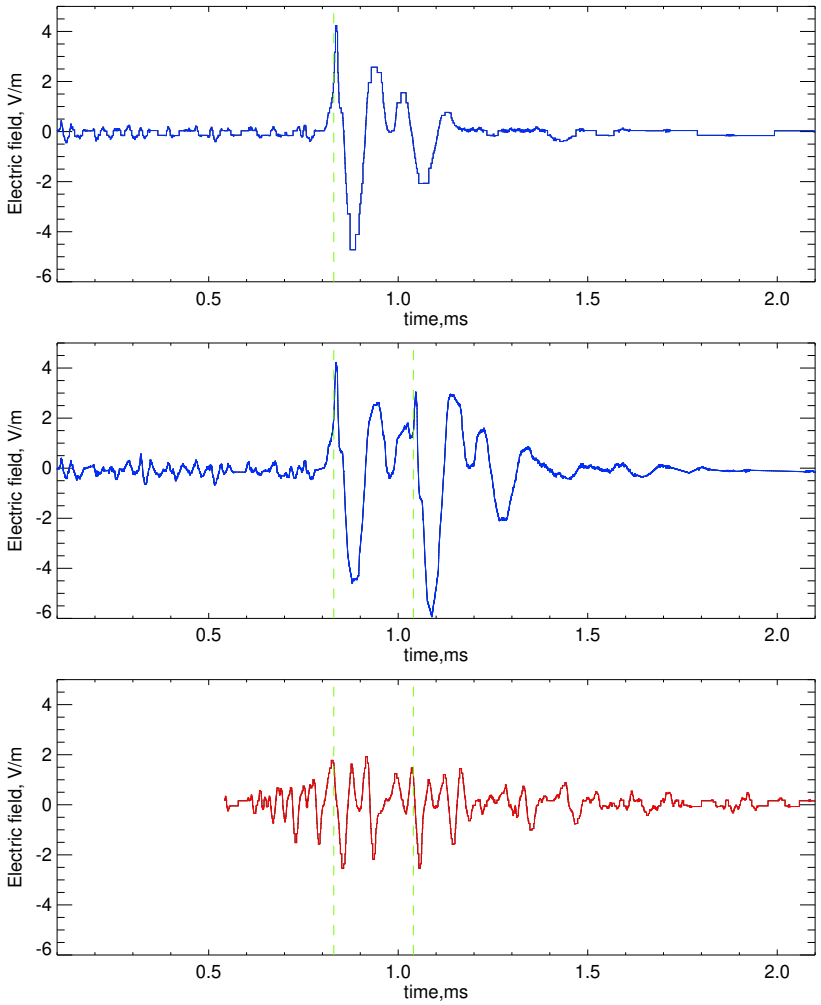

Figure 3.12: Top: Event 3 waveform inverted. Middle: Two inverted Event 3 waveforms separated by 210 μs and summed. Bottom: Event 2 waveform.

but the behavior appears to match and may explain Event 2's multiple pulses at equally high peak current.

The final enigma of Event 2 is its clear positive polarity. The ENTLN sensors classified this lightning event as being a +IC, which describes an intra-cloud leader channel

moving negative charge upward. Depending on the source altitude of the TGF, which is unknown, this could be a reverse beam observation from the ground as first modeled in Ortberg et al. (2020). It is also possible that the event was lateral to or lower in altitude with respect to the observation point (2.5 km) making the main beam visible to the Tower and instrument. A detailed meteorological analysis of the storm and its possible charge structure and altitudes would need to be done to begin to answer this question.

3.5 Conclusion

The vast majority of TGFs have been detected by spaced-based instruments [Fishman et al. 1994; Smith et al. 2005; Briggs et al. 2010; Marisaldi et al. 2010; Østgaard et al., 2019; Neubert et al. 2020] and are dominated by associations with positive IC lightning leaders. TGFs however have turned out to be linked to a wide variety of lightning types and atmospheric conditions, as evidenced by these unique Mt. Santis events and the numerous ground based observations of downward directed TGFs [Dwyer et al. 2003a/2004; Tran et al. 2015; Hare et al. 2016; Bowers et al. 2017; Enoto et al. 2017; Colalillo, 2017; Smith et al. 2018; Abbasi et al. 2022; Wada et al. 2022].

As challenging as ground observations are, the potential to observe the finer details of the relationship between the gamma ray fluence and the lightning leader current fluctuations cannot be overstated. Though orbital observations have provided large data

sets and continue to contribute to our understanding of the TGF mechanism there are clear advantages to observations made within a few km's of the TGF source. They include the ability to observe the varied particle physics associated with TGFs such as photo-neutrons [Bowers et al. 2017], positrons, and certain radio active decay elements [Enoto et al. 2017]. As speculated in this paper it may also be possible to observe stepped leader emissions that precede and are possibly integral to the TGF mechanism.

A further possibility of ground or airborne observations is obtaining photon arrival time distributions unaffected by the 100's of km's of atmospheric transport between storm cloud altitudes and orbital space craft with sufficient numbers of counts to be statistically robust. These 'in-situ' observations could help determine if there is an underlying behavior of discrete bursts of emission in the overall TGF time profile. As of November 2021 one of the six THOR instruments developed by the high energy atmospheric physics group at the University of California Santa Cruz has been deployed to the base of the Säntis Tower and the other five have been deployed elsewhere around the globe including Japan, New Mexico and Florida. We hope that over the next few years the observations made by these instruments, along with radio sferic data, will contribute to a greater understanding of the lightning-TGF relationship.

Section 4

Instrumentation and Future Research

Over the course of my undergraduate and graduate education I have gained extensive experience with the design and development of advanced sensing instruments for x-ray, gamma-ray, and neutron particle detection. I began designing detectors at the undergraduate level as the science lead for a solar physics cubesat at the University of Minnesota Small Satellite Research Laboratory (SSRL). This instrument, shown in Figure 4.1, has since been launched into orbit from the International Space Station in February 2020.

As a graduate student I shifted my focus from solar to terrestrial radiation, notably the Terrestrial Gamma-ray Flash (TGF). In my time at UCSC working with Dr. David Smith I have completed numerous instrument projects and deployments. I collaborated on a balloon instrument payload, the Light And Fast TGF Recorder (LAFTR) detector (Figure 4.2). I built and wrote software for a single detector instrument (Figure 4.3) that was our first deployment to the Säntis Tower in Switzerland and netted us

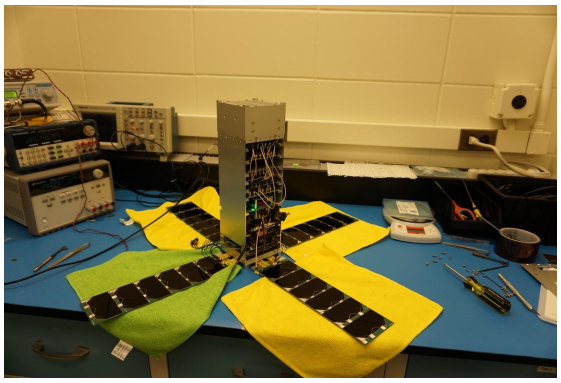

Figure 4.1: Minnesota Small Satellite Research Laboratory (SSRL) CubeSat. Scientific instrument is in the upper enclosed portion of the space craft and is an X-ray sensor intended to be a proof of concept for solar observations using low cost small sat technologies. The instrument consisted of 8 thalium doped cesium iodide crystals mounted to silicon photo-multipliers (SiPM) devices with charge sensitive pre-amplification and shaping. This CubeSat was launched into orbrit from the ISS in February of 2020.

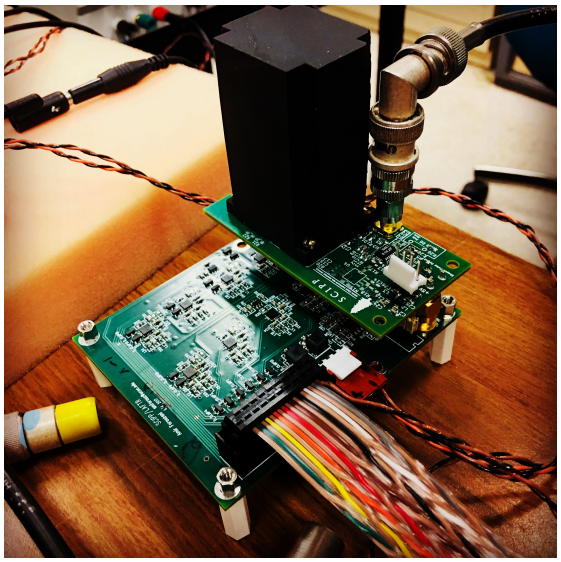

Figure 4.2: Analog portion of the Light and Fast TGF Recorder (LAFTR). Black housing contains a cube of scintillation material mounted to a silicon photo multiplier. Future balloon deployments are in the works for this instrument.

three TGF detections resulting in one of my first publications. My largest hardware contribution was being a principal graduate student researcher in the development of the Terrestrial High-energy Observations of Radiation (THOR) project (Figure 4.4),

funded through an Air Force Office of Scientific Research instrumentation grant. With this project, intended for ground and airborne based TGF observations, we developed a set of six instruments. Each one includes a four detector array using different size and material scintillation crystals mounted to traditional photo-multiplier devices. Each detector is equipped with GPS pulse per second timing and has the capability of saving limited amounts of triggered PMT trace data along with a continuous list mode data aquisition, i.e. photon energy (integrated PMT pulse) and timestamp. through the fall

Figure 4.3: A single 5"×5" plastic scintillator mounted to a photo multiplier with accompanying high voltage and singal processing electronics. This instrument was first deployed at the Säntis Tower in Switzerland during 2020 and 2021. It is currently deployed on the Dalmatian coast in Splitt, Croatia.

of 2021 and spring 2022 we have deployed the THOR instruments around the world including Japan (West Coast in Winter, Mt. Fuji in summer), Switzerland (Säntis Tower), Florida (Florida Institute of Technology), New Mexico (Langmuir Laboratory and Los Alamos Laboratory) and aboard the National Oceanic and Atmospheric Administration (NOAA) Hurricane hunter aircraft. We also moved our initial low-cost instrument from Säntis Switzerland to Split, Croatia to observe winter lightning from the Mediterranean

Sea.

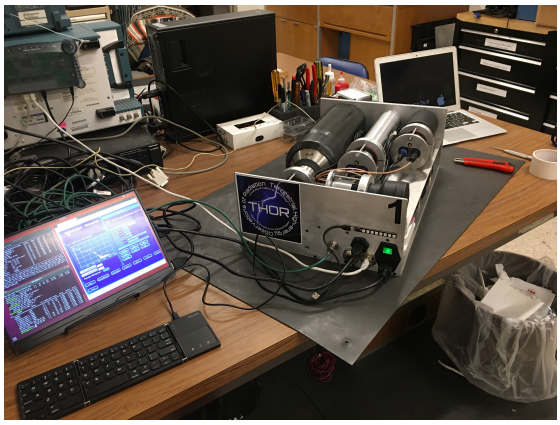

Figure 4.4: The Terrestrial High-energy Observations of Radiation (THOR) instrument consists of a four detector array, three plastic of varying size and one Sodium Iodide, each mounted to a photo-multiplier tube (PMT). The analog shaping and digitizing electronics are incorporated into the high voltage base of the PMTs. The shaped waveform is sampled by a 80 MHz ADC with an FPGA acquiring and managing the data and maintaining the high voltage bias. The detector electronics interface with the instrument computer via USB 1.2, and the 5V USB hub power is used by the detector base to supply the necessary high voltage to the PMTs. There are six of these instruments currently deployed around the world.

Throughout 2022 I worked in the Intelligence and Space Research - Space Science and Applications Group (ISR-1) at Los Alamos National Laboratory (LANL) to design and build 10 dual-sensor instruments, Airborne Detection Of Thunderstorm Radiation (ADOTR), (Figure 4.5) that will provide high energy detection aboard aircraft as part of the United States Air Force Weather Reconnaissance Program. The design is based on THOR but with updated electronics and firmware. This project has led to a postdoctoral appointment with the Air Force Institute of Technology (AFIT) where I will be continuing with high energy atmospheric physics research as a member of the group deploying the 10 instruments mentioned previously.

Just like THOR the ADOTR instruments are capable of saving limited amounts

Figure 4.5: The Airborne Detection Of Thunderstorm Radiation (ADOTR) instruments consist of a two detector array. The array consist of one plastic scintillator and one sodium iodide scintillator each mounted to a photo-multiplier tube (PMT). The analog shaping and digitizing electronics are incorporated into the high voltage base of the PMTs. The shaped waveform is sampled by a 40 MHz ADC with an FPGA acquiring and managing the data, while an ARM processor controls the PMT and executes gain and performance stabilization. The detector electronics interface with the instrument computer via USB 1.2, and the 5V USB hub power is used by the detector base to supply the necessary high voltage to the PMTs. A total of 10 instruments are being deployed on separate C-130 USAF Hurricane Hunter Aircraft.

of trace data when triggered with TGF like count rates. This capability will be instrumental in answering questions about the time domain of the TGF signal, i.e. a smooth time profile of photon arrival or multiple discrete bursts? When we observe the TGF from close proximity (1-2 km) do we consistently see a burst of stepped leader emission prior to the main TGF? This capability along with the number of ground/airborne instruments deployed for TGF research by our two collaborating groups is going to generate more data of in-situ TGF observations in the next couple years then has been seen in the last decade. As a postdoc with AFIT I will continue to be involved with THOR and Dr. Smith's research group and I am excited for the possibility of strong

collaborations between UCSC and AFIT on analysis and publications.

Bibliography

[1] Abbasi et al. (2018) "Gamma Ray Showers Observed at Ground Level in Coincidence With Downward Lightning Leaders". JGR, Vol. 13, 6864.

[2] Abbasi et al. (2022) "First High-speed Camera Observations of the Optical Counterpart of a Terrestrial Gamma-ray Flash". eprint arXiv:2205.05115

[3] Agostinelli, S., Allison, J., Amako, K., Apostolakis, J., Araujo, H., Arce, P., et al. (2003) GEANT4 - a simulation toolkit. Nuclear Instruments and Methods in Physics Research A, 506(3), 250–303. https://doi.org/10.1016/S0168-9002(03)01368-8

[4] Allison, J., Amako, K., Apostolakis, J., Araujo, H., Arce Dubois, P., Asai, M., et al. (2006). Geant4 developments and applications. IEEE Transactions on Nuclear Science, 53(1), 270–278. https://doi.org/10.1109/TNS.2006.869826

[5] Allison, J., Amako, K., Apostolakis, J., Arce, P., Asai, M., Aso, T., et al. (2016) Recent developments in GEANT4.d Nuclear Instruments and Methods in Physics Research A, 835, 186–225. https://doi.org/10.1016/j.nima.2016.06.125

[6] .L.P. Babich, E.N. Donskoy, I.M. Kutsyk, R.A. Roussel-Dupré.(2005) The feedback mechanism of runaway air breakdown Geophys. Res. Lett. 32, L09809

[7] Babich, L. P. (2006) Generation of neutrons in giant upward atmospheric discharges. Soviet Journal of Experimental and Theoretical PhysicsLetters,84, 285–288.

[8] Babich, L. P. (2007) Neutron generation mechanism correlated with lightning discharges. Geomagnetism and Aeronomy,47, 664–670.

[9] Bhat (2016) The Third Fermi GBM Gamma-Ray Burst Spectral Catalogue: Six Years of Data. The Astrophysical Journal Supplement Series, 223:2, 2016 April

[10] Bowers et al. (2017) "Gamma-ray signatures of neutrons from a terrestrial gamma-ray flash". Geophysical Research Letters, doi: 10.1002/2017GL075071

[11] Bowers et al. (2018) "A Terrestrial Gamma-Ray Flash inside the Eyewall of Hurricane Patricia". Geophysical Research Letters, doi: 10.1029/2017JD027771

[12] Briggs, M. S., et al. (2010) First results on terrestrial gamma ray flashes from the Fermi Gamma-ray Burst Monitor J. Geophys. Res., 115, A07323, doi:10.1029/2009JA015242

[13] Briggs et al.(2013) Terrestrial Gamma Ray Flashes in the Fermi era:Improved Observations and Analysis Methods. JGR Space Physics: Vol 118 3805-3830.

[14] Carlson, B. E., Lehtinen, N. G., & Inan, U. S. (2010). Terrestrial gamma ray flash production by lightning current pulses. Journal of Geophysical Research, 114, A00E08. https://doi.org/10.1029/2009JA014531

[15] Celestin, S., Pasko, V. P. (2011). Energy and fluxes of thermal runaway electrons produced by exponential growth of streamers during the stepping of lightning leaders and in transient luminous events. Journal of Geophysical Research, 116, 3315. https://doi.org/10.1029/2010JA016260

[16] Chen et al. (2008) Global distributions and occurrence rates of transient luminous events J. Geophys. Res. 113, A08306

[17] Cohen et al. (2006) Terrestrial gamma ray flashes observed aboard the Compton Gamma Ray Observatory/Burst and Transient Source Experiment and ELF/VLF radio atmospherics. Journal of Geophysical Research: Atmospheres, 111, D24109.

[18] Colalillo, R. (2017) "Peculiar lightning-related events observed by the surface detector of the Pierre Auger Observatory". In Proceedings of 35th International Cosmic Ray Conference — PoS(ICRC2017). https://doi.org/10.22323/1.301.0314

[19] Colalillo et al. on behalf of the Pierre Auger Collaboration (2021) Downward Terrestrial Gamma-ray Flashes at the PierreAuger Observatory? In Proceedings of 37th International Cosmic Ray Conference, DOI:10.22323/1.395.0395

[20] Collier et al. (2011) Assessing the power law distribution of TGFs. Journal of Geophysical Research, 116, A10320.

[21] Connaughton et al. (2010) Associations between Fermi Gamma-ray Burst Monitor terrestrial gamma ray flashes and sferics from the World Wide Lightning Location Network. Journal of Geophysical Research, 115, A12307.

[22] Cooray V. (2003) Mechanism of Electrical Discharges Chapter 3: The Lightning Flash. The Institute of Electrical Engineers, 2003 ISBN 0 85296 780 2

[23] Cooray V. (2015) An Introduction to Lightning. Springer Dordrecht, ISBN 978-94-017-8937-0, https://doi.org/10.1007/978-94-017-8938-7

[24] Cummer et al. (2005) Measurements and implications of the relationship between lightning and terrestrial gamma ray flashes. Geophysical Research Letters, 32, L08811.

[25] Cummer et al. (2011) "The lightning-TGF relationship on microsecond timescales". Geophysical Research Letters, 38, L14810. https://doi.org/10.1029/2011GL048099

[26] Cummer et al. (2014) "The source altitude, electric current, and intrinsic brightness of terrestrial gamma ray flashes". Geophysical Research Letters 41 , pages 8586-8593, doi:10.1002/2014GL062196

[27] Cummer et al. (2017) The connection between terrestrial gamma-ray flashes and energetic in-cloud lightning pulses. AGU 2017 Fall Meeting, New Orleans, LA.

[28] Dowell et al. (2022) "The High-Resolution Rapid Refresh (HRRR): An Hourly Updating Convection-Allowing Forecast Model. Part I: Motivation and System Description". https://doi.org/10.1175/WAF-D-21-0151.1, AMS Journals

[29] Joseph Dwyer (2003) A fundamental limit on electric fields in air. Geophys. Res. Lett. 30, 2055

[30] Dwyer, J. R., et al. (2003a) Energetic radiation produced during rocket-triggered lightning. Science, 299, 694–697.

[31] Dwyer et al. (2004) A ground level gamma-ray burst observed in association with rocket-triggered lightning. Geophysical Research Letters 31(5) DOI:10.1029/2003GL018771

[32] Dwyer, J. R., and D. M. Smith (2005) A comparison between Monte Carlo simulations of runaway breakdown and terrestrial gamma-ray flash observations. Geophys. Res. Lett., 32, L22804, doi:10.1029/2005GL023848.

[33] Dwyer, J. R. (2007) Relativistic breakdown in planetary atmospheres. Physics of Plasmas, 14(4), 042901–042,901. https://doi.org/10.1063/1.2709652

[34] Joseph Dwyer (2008) Source mechanisms of terrestrial gamma-ray flashes. Geophys. Res. 113(D10), D10103

[35] Joseph Dwyer, David Smith, and Steven Cummer. (2012) High−Energy Atmospheric Physics: Terrestrial Gamma-Ray Flashes and Related Phenomena. Space Sci Rev (2012) 173:133–196 DOI 10.1007/s11214-012-9894-0

[36] Joseph R. Dwyer,Steven A. Cummer (2013) Radio emissions from terrestrial gamma-ray flashes. JGR Space Physics, Volume118, Issue6, https://doi.org/10.1002/jgra.50188

[37] Joseph Dwyer and Marin Uman. (2014) The Physics of Lightning. In Physics Reports 534 (2014) 147–241

[38] Dwyer et al. (2017) "Characterizing the source properties of terrestrial gamma ray flashes". JGR space physics, https://doi.org/10.1002/2017JA024141

[39] Enoto et al. (2017) "Photonuclear reactions triggered by lightning discharge". Nature 551, 481–484. https://doi.org/10.1038/nature24630

[40] Fishman et al. (1994) "Discovery of intense gamma-ray flashes of atmospheric origin". Science, 264(5163), 1313–1316.

[41] Fermi Gamma Ray Burst Monitor Terrestrial Gamma-ray Flash (TGF) Catalog. https://fermi.gsfc.nasa.gov/ssc/data/access/gbm/tgf/

[42] Foley et al. (2014) Pulse properties of terrestrial gamma-ray flashes detected by the Fermi Gamma-Ray Burst Monitor. JGR Space Physics, Volume 119, Issue 7, Pages 5931-5942

[43] Gjesteland, T., Østgaard, N., Laviola, S., Miglietta, M. M., Arnone, E., Marisaldi, M., Fuschino, F., Collier, A. B., Fabró, F., Montanya, J. (2015) Observation of intrinsically bright terrestrial gamma ray flashes from the Mediterranean basin. Journal of Geophysical Research: Atmospheres, 120, 12,143–12,156. https://doi.org/10.1002/2015JD023704

[44] Gjesteland et al. (2017) On the timing between terrestrial gamma ray flashes, radio atmospherics, and optical lightning emission. Geophysical Research Letters, Volume 122, Issue 7, https://doi.org/10.1002/2017JA024285

[45] Grefenstette, B. W., D. M. Smith, B. J. Hazelton, and L. I. Lopez (2009), First RHESSI terrestrial gamma ray flash catalog, J. Geophys. Res., 114, A02314,

[46] Griffiths, R. F., Phelps, C. T. (1976) A model for lightning initiation arising from positive corona streamer development. Journal of Geophysical Research, 81(21), 3671–3676.

[47] David Gruber. (2014) The First Fermi GBM Gamma-Ray Burst Spectral Catalogue: Four Years of Data. The Astrophysical Journal Supplement Series, 211:12, 2014 March

[48] A.V. Gurevich. (1961) On the theory of runaway electrons. Sov. Phys. JETP 12(5), 904–912 (1961)

[49] A.V. Gurevich, G.M. Milikh, and R.A. Roussel−Dupre. (1992) Runaway electron mechanism of air breakdown and preconditioning during a thunderstorm Phys. Lett. A 165, 463 (1992)

[50] Gurevich et al. (2000) "Generation of electron-positron pairs in runaway breakdown". Phys. Lett. A, 275, 101–108, 2000.

[51] A.V. Gurevich, K.P. Zybin. (2001) Runaway breakdown and electric discharges in thunderstorms Phys. Usp. 44, 1119 (2001)

[52] Hare, B. M., Uman, M. A., Dwyer, J. R., Jordan, D. M., Biggerstaff, M. I., Caicedo, J. A.,...Bozarth, A. (2016). Ground-level observation of a terrestrial gamma ray

flash initiated by a triggered lightning. Journal of Geophysical Research: Atmospheres,121, 6511–6533 https://doi.org/10.1002/2015JD024426

[53] B.J. Hazelton, (2009) PhD dissertation, University of California, Santa Cruz (2009)

[54] Jayaratne et al. (1983) "Laboratory studies of the charging of soft-hail during ice crystal interactions". Quarterly Journal of the Royal Meteorological Society, https://doi.org/10.1002/qj.49710946111

[55] Andreas von Kienlin.(2014) The Second Fermi GBM Gamma-Ray Burst Spectral Catalogue: Four Years of Data. The Astrophysical Journal Supplement Series, 211:13, 2014 March

[56] Lehtinen, N. G., Walt, M., Inan, U. S., Bell, T. F., Pasko, V. P. (1996) Gamma-ray emission produced by a relativistic beam of runaway electrons accelerated by quasi-electrostatic thundercloud fields. Geophysical Research Letters, 23, 2645–2648.

[57] Lindanger et al. (2022) Production of Terrestrial Gamma-Ray Flashes During the Early Stages of Lightning Flashes. Journal of Geophysical Research: Atmospheres, 127, e2021JD036305. https://doi.org/10.1029/2021JD036305

[58] Lu et al., (2011) Characteristics of broadband lightning emissions associated with terrestrial gamma ray flashes. Journal of Geophysical Research, Volume 116, Issue A3, https://doi.org/10.1029/2010JA016141

[59] Lyu, F., S. A. Cummer, and L. McTague (2015) Insights into high peak current

in-cloud lightning events during thunderstorms. Geophys. Res. Lett., 42, 6836–6843, doi:10.1002/2015GL065047.

[60] Lyu et al. (2016) "Ground detection of terrestrial gamma ray flashes from distant radio signals". Geophysical Research Letters, 43, 8728–8734. https://doi.org/10.1002/2016GL070154

[61] Lyu, F., Cummer, S. A., Briggs, M. S., Smith, D. M., Mailyan, B., Lesage, S. (2021)a. Terrestrial gamma-ray flashes can be detected with radio measurements of energetic in-cloud pulses during thunderstorms. Geophysical Research Letters, 48, e2021GL093627. https://doi. org/10.1029/2021GL093627

[62] Lyu et al. (2021)b A Distinct Class of High Peak Current Lightning Pulses Over Mountainous Terrain in Thunderstorms. Geophysical Research Letters, 48, e2021GL094153. https://doi. org/10.1029/2021GL094153

[63] Mailyan et al. (2016) The spectroscopy of individual terrestrial gamma-ray flashes: Constraining the source properties. JGR Space Physics, Volume 121, Issue 11, Pages 11,346-11,363

[64] Marisaldi et al. (2010) Detection of terrestrial gamma rayflashes up to40 MeV by the AGILE satellite. Journal of Geophysical Research,115, A00E13

[65] Marshall, T. C., and W. D. Rust (1991) Electric field soundings through thunderstorms. Geophys. Res., 96, 22,297.

[66] Marshal et al. (2013) Initial breakdown pulses in intracloud lightning flashes and

their relation to terrestrial gamma ray flashes. Geophysical Research Letters, Volume 118, Issue 19, https://doi.org/10.1002/jgrd.50866

[67] Moss, G. D., Pasko, V. P., Liu, N., Veronis, G. (2006). Monte Carlo model for analysis of thermal runaway electrons in streamer tips in transient luminous events and streamer zones of lightning leaders. Journal of Geophysical Research, 111, A02307. https://doi.org/10.1029/2005JA011350

[68] Neubert et al., (2020) A terrestrial gamma-ray flash and ionospheric ultraviolet emissions powered by lightning. SCIENCE 12 Dec 2019 Vol 367, Issue 6474 pp. 183-186 DOI: 10.1126/science.aax3872

[69] Ortberg et al. (2020) Detecting an Upward Terrestrial Gamma Ray Flash from its Reverse Positron Beam. JGR Atmospheres, Volume 125, Issue 6, e2019JD030942, https://doi.org/10.1029/2019JD030942

[70] Østgaard et al. (2012) "The true fluence distribution of terrestrial gamma flashes at satellite altitude". 24 March 2012 https://doi.org/10.1029/2011JA017365

[71] Østgaard et al. (2013) Simultaneous observations of optical lightning and terrestrial gamma ray flash from space Geophysical Research Letters, Volume 40, Issue 10, 2423-2426, https://doi.org/10.1002/grl.50466

[72] Østgaard et al. (2019) The Modular X- and 1 Gamma- ray Sensor (MXGS) of the ASIM payload on the International Space Station. Space Sci. Rev. 215, 23

[73] Pu et al. (2019) Low Frequency Radio Pulses Produced by Terrestrial Gamma-Ray Flashes. Geophysical Research Letters, Volume46, Issue12 Pages 6990-6997, https://doi.org/10.1029/2019GL082743

[74] Pu et al. (2020) A Satellite-Detected Terrestrial Gamma Ray Flash Produced by a Cloud-to-Ground Lightning Leader Geophysical Research Letters, Volume47, Issue15, 16 August 2020, e2020GL089427

[75] Vladimir Rakov and Martin Uman. (2003) "Lightning Physics and Effects". Cambridge University Press

[76] David M. Smith et al., (2002) The RHESSI Spectrometer J. Geophys. Res. 116, D20124

[77] Smith et al. (2005) Terrestrial Gamma-Ray Flashes Observed up to 20 MeV. SCIENCE 18 Feb 2005Vol 307, Issue 5712pp. 1085-1088 DOI: 10.1126/science.1107466

[78] Smith et al., (2010) High spatial resolution correlation of AGILE TGFs and global lightning activity above the equatorial belt, J. Geophys. Res. A 115, A00E49

[79] Smith et al. (2018) "Characterizing upward lightning with and without a terrestrial gamma ray flash". Journal of Geophysical Research: Atmospheres, 123, 11,321–11,332. https://doi.org/10.1029/ 2018jd029105

[80] Smith et al. (2020) Special Classes of Terrestrial Gamma Ray Flashes From RHESSI. JGR Atmospheres, Volume 125, Issue 20, e2020JD033043, https://doi.org/10.1029/2020JD033043

[81] Somu et al. (2015) A study of changes in apparent ionospheric reflection height within individual lightning flashes. Journal of Atmospheric and Solar-Terrestrial Physics, 136(D20), DOI:10.1016/j.jastp.2015.09.007

[82] Stanley et al. (2006) A link between terrestrial gamma-ray flashes and intracloud lightning discharges. Geophysical Research Letters, 33, L06803.

[83] Stolzenburg et al. (2007) Electric field values observed near lightning flash initiations. Geophysical Research Letters, Volume 34, issue 4.

[84] Takahashi (1978) "Riming Electrification as a Charge Generation Mechanism in Thunderstorms". Journal of the Atmospheric Sciences. https://doi.org/10.1175/1520-0469(1978)035¡1536:REAACG¿2.0.CO;2

[85] Taranenko, Y., and R. Roussel-Dupré (1996) "High altitude discharges and gamma-ray flashes: A manifestation of runaway air breakdown". Geophys. Res. Lett., 23, 571–574, doi:10.1029/95GL03502.

[86] Tierney et al. (2013) "Fluence distribution of terrestrial gamma ray flashes observed by the Fermi Gamma-ray Burst Monitor". JGR Space Physics. https://doi.org/10.1002/jgra.50580

[87] Tran et al. (2015) "A terrestrial gamma-ray flash recorded at the Lightning Observatory in Gainesville, Florida". 1 December 2015, Journal of Atmospheric and Solar-Terrestrial Physics

[88] Y. Wada, T. Enoto, K. Nakazawa, Y. Furuta, T. Yuasa, Y. Nakamura, T. Morimoto, T. Matsumoto, K. Makishima, and H. Tsuchiya (2019a) Downward Terrestrial Gamma-Ray Flash Observed in a Winter Thunderstorm. Phys. Rev. Lett. 123, 061103 – Published 7 August 2019

[89] Wada et al. (2019b) Gamma-ray glow preceding downward terrestrial gamma-ray flash. Communications Physics volume 2, Article number: 67 (2019)

[90] Wada et al. (2020) High Peak-Current Lightning Discharges Associated With Downward Terrestrial Gamma-Ray Flashes. Geophysical Research Letters, Volume125, Issue4, e2019JD031730, https://doi.org/10.1029/2019JD031730

[91] Wada et al. (2022) "Characteristics of Low-Frequency Pulses Associated With Downward Terrestrial Gamma-Ray Flashes". Geophysical Research Letters. 28 February 2022, https://doi.org/10.1029/2021GL097348

[92] Williams et al. (2006) Lightning flashes conducive to the production and escape of gamma radiation to space, J. Geophys. Res. D 111, D16209

[93] C.T.R. Wilson. (1925) The acceleration of beta particles in strong electric fields such as those of thunderclouds Cambridge Philol. Soc. 22, 534–538

[94] Zhu et al. (2016) A study of National Lightning Detection Network responses to natural lightning based on ground truth data acquired at LOG with emphasis on cloud discharge activity. JGR Atmospheres, Volume 121, Issue 24, Pages 14,651-14,660